

Contents lists available at ScienceDirect

Petroleum Science

journal homepage: www.keaipublishing.com/en/journals/petroleum-science



Original Paper

A novel intermingled fractal model for predicting relative permeability in tight oil reservoirs considering microscopic pore geometry



You Zhou a,b, Song-Tao Wu b,*, Ru-Kai Zhu b, Xiao-Hua Jiang b, Gan-Lin Hua c

- ^a School of Civil Engineering, Hebei University of Engineering, Handan, 056038, Hebei, China
- ^b PetroChina Research Institute of Petroleum Exploration & Development, Beijing, 100083, China
- ^c China Petroleum Enterprise Association, Beijing, 100120, China

ARTICLE INFO

Article history: Received 12 March 2025 Received in revised form 26 April 2025 Accepted 19 June 2025 Available online 26 June 2025

Edited by Xi Zhang and Jie Hao

Keywords: Tight oil reservoirs Intermingled fractal Pore geometry Relative permeability Hydraulic diameter

ABSTRACT

Accurately predicting relative permeability is an important issue in the research of multiphase flow in tight reservoirs. Existing predictive models typically rely on the capillary tube bundle model featuring circular cross-sections, often overlooking the impact of pore geometry on fluid flow behavior within reservoirs. In this work, the intermingled fractal theory of porous media is introduced to characterize the intricate local features within the internal space of tight rocks. Initially, iterative rules for diverse fractal units are skillfully designed to capture the actual characteristics of pore cross-sectional shapes. Subsequently, analytical relationships are derived between the iterative parameters and the area, wetted perimeter, and hydraulic diameter of pores generated by these units, followed by the establishment of a relative permeability model that considers pore geometry. The model's validity is confirmed through comparisons with experimental data and published relative permeability models, with correlation coefficients exceeding 0.996. Finally, various factors affecting two-phase flow characteristics are analyzed. The results reveal that pore geometry has a significant impact on flow behavior in porous media. Assuming that the flow channels are cylindrical typically leads to an overestimation of permeability, with the maximum relative error reaching 46.91%. Additionally, the tortuosity fractal dimension is a determinant factor influencing the relative permeability of both wetting and nonwetting fluids, and the phase permeability is sensitive to variations in solid particle size and porosity. The proposed intermingled fractal model enhances the accuracy of evaluating fluid flow characteristics in microscale pore channels and offers a novel framework for simulating porous media with complex

© 2025 The Authors. Publishing services by Elsevier B.V. on behalf of KeAi Communications Co. Ltd. This is an open access article under the CC BY-NC-ND license (http://creativecommons.org/licenses/by-nc-nd/4.0/).

^{*} Corresponding author.

E-mail addresses: wust@petrochina.com.cn, rock.geoscience@outlook.com (S.-T. Wu).

Peer review under the responsibility of China University of Petroleum (Beijing).

Nomeno	clature	q	Flow rate through a single capillary $(10^{-9} \text{ m}^3/\text{s})$		
			Flow rate of the non-wetting phase fluid through a		
Α	Cross-sectional area of the capillary (µm²)		single capillary $(10^{-9} \text{ m}^3/\text{s})$		
A(i)	Area of the <i>i</i> -th level pore (μm^2)	$q_{ m w}$	Flow rate of the wetting phase fluid through a single		
$A(i)_m$	Area of the <i>i</i> -th level pore given a total number of	***	capillary $(10^{-9} \text{ m}^3/\text{s})$		
. ,	iterations of $m (\mu m^2)$	Q	Total flow rate through a unit cell $(10^{-9} \text{ m}^3/\text{s})$		
$A_{\rm p}$	Generated cumulative pore area (µm²)	Q_{nw}	Total flow rate of the non-wetting phase fluid		
A_{t}^{p}	Cross-sectional area of the REV (μ m ²)	Ciw	through a unit cell $(10^{-9} \text{ m}^3/\text{s})$		
d_{av}	Average hydraulic diameter (µm)	Q_{w}	Total flow rate of the wetting phase fluid through		
d_e	Equivalent circle diameter (µm)	CVV	unit cell $(10^{-9} \text{ m}^3/\text{s})$		
$d_{ m h}$	Hydraulic diameter (µm)	r	Pore radius (µm)		
$d_{\rm h}(i)_m$	Hydraulic diameter of the <i>i</i> -th level pore given a total	r_0	1st-level solid particle radius (µm)		
u _{n(t)m}	number of iterations of m (μ m)	r _i i-th	level solid particle radius (µm)		
$d_{ m h,nw}$	Hydraulic diameter of the non-wetting phase (μ m)	S_{A}	Total area of fractal unit A (μ m ²)		
$d_{h,nw}$	Hydraulic diameter of the wetting phase (µm)	$S_{\rm in}(i)$	Area of the inner pore enclosed by i -th level solid		
и _{н,w} Dт	Average tortuosity fractal dimension	$J_{\rm in}(t)$	particles (μ m ²)		
-	Average tortuosity fractal dimension of the non-	S_{nw}	Saturation of the non-wetting phase (%)		
$D_{T,nw}$	wetting phase		Area of the edge pore enclosed by i -th level solid		
D		$S_{\rm out}(i)$			
$D_{T,w}$	Average tortuosity fractal dimension of the wetting	C	particles (µm²)		
	phase	$S_{\mathbf{w}}$	Saturation of the wetting phase (%)		
i	Arbitrary number of iterations	ν	Flow velocity (10 ³ m/s)		
Ka	Absolute permeability (mD)	V_{nw}	Volume occupied by the non-wetting phase fluid		
K_{nw}	Permeability of the non-wetting phase (mD)		(μm^3)		
K_{rnw}	Relative permeability of the non-wetting phase	$V_{ m p}$	Pore volume (µm³)		
K_{rw}	Relative permeability of the wetting phase	λ	Pore diameter (µm)		
K_{w}	Permeability of the wetting phase (mD)	ϕ	Porosity (%)		
L_0	Edge length of the REV (μm)	ϕ_{A}	Porosity of fractal unit A (%)		
$L_{\rm in}(i)$	Length of a single side of the inner pore enclosed by	δ	Shape factor		
	i-th level solid particles (μm)	σ	Surface tension		
$L_{out}(i)$	Length of a single side of the edge pore enclosed by i-	μ	Fluid viscosity at an arbitrary point (mPa·s)		
	th level solid particles (µm)	μ_0	Fluid inherent viscosity (mPa·s)		
L_{t}	Actual length of the curved capillary (µm)	$\mu_{0,\mathrm{nw}}$	inherent viscosity of the non-wetting phase fluid		
m	Total number of iterations		(mPa·s)		
n_i	Number of <i>i</i> -th level pores	$\mu_{0,W}$	inherent viscosity of the wetting phase fluid (mPa-		
N	Number of fractal units	$ au_{av}$	Average tortuosity		
$N_{\rm n}$	Number of solid particles excluded from each	Δp	Driving pressure difference (MPa)		
••	iteration	BSEI	Backscattered electron images		
N_s	Number of solid particles involved in each iteration	CPSD	Cumulative pore size distribution		
P	Wetted perimeter (µm)	IFM	Intermingled fractal model		
P(i)	Perimeter of the <i>i</i> -th level pore (µm)	IFU	Intermingled fractal unit		
$P(i)_m$	Perimeter of the <i>i</i> -th level pore given a total number	MAPS	Modular automated processing system		
- (*)111	of iterations of m (μm)	MICP	Mercury injection capillary pressure		
$P_{\rm in}(i)$	<i>i</i> -th level inner pore	PSD	Pore size distribution		
$P_{\text{out}}(i)$	<i>i</i> -th level edge pore	REV	Representative volume element		

1. Introduction

The investigation of two-phase flow in porous media has significant scientific and practical implications, with wide applications across various fields (Liao et al., 2024; Ma et al., 2024; Nimvari et al., 2024). In oil and gas development, relative permeability is a crucial parameter that comprehensively characterizes the flow capacity of different fluids in the rock. As a result, accurately determining relative permeability has become a key research focus (Juri et al., 2016; Yu et al., 2024). However, the extreme complexity and irregularity of the pore structure in tight reservoir rocks make it difficult to obtain relative permeability. Compared to conventional formation, the various microscale effects in tight oil reservoirs further complicate understanding the

transport mechanisms of two-phase flow (Wang et al., 2017; Huang et al., 2018). Therefore, developing a simple and effective method to determine the relative permeability of dense rocks has become a critical issue that requires urgent attention in current research.

Studies have shown that fractal theory is an effective mathematical tool for describing pore structure and fluid flow characteristics. In recent years, significant progress has been made in two-phase flow research using fractal theory. Zhao et al. (2024) proposed a fractal seepage model that considers both irreducible fluid saturation and stress effects, which demonstrated strong predictive capability for the relative permeability of rocks. Li et al. (2022b) developed a relative permeability model for unsaturated shale, considering variations in parameters such as nanopore

wettability and viscosity. Chai et al. (2024) proposed a new oilwater two-phase relative permeability model based on fractal theory, which incorporates stress sensitivity. The results indicate that irreducible water and residual oil saturation are negatively correlated with effective stress, and the region of co-infiltration decreases as effective stress increases. Sun et al. (2025) proposed a fractal model of relative permeability for waterflooding in rough fractures, which was validated by comparison with numerical results. These studies demonstrate the potential of fractal theory in describing multiphase flow characteristics. In contrast to relative permeability models derived from experiments or numerical simulations, the fractal model offers the advantage of expressing relative permeability as a function of structural parameters of porous media, without empirical constants, and each parameter has a clear physical meaning (Chen et al., 2020; Wang et al., 2023; Yang et al., 2024).

With the development of fractal geometry, it is increasingly recognized that real porous media exhibit multifractal characteristics (Fu et al., 2022; Wang et al., 2024; Wei et al., 2025), and characterizing such media with only monofractal may overlook many important details. Especially for tight oil reservoirs, the diverse shapes and types of pores within the rock make it difficult to simplify this heterogeneity using a monofractal approach (Zhou et al., 2018). As a result, many researchers have explored the intermingled fractal theory based on monofractal. The concept of intermingled fractal was first proposed by Atzeni et al. (2008) and progressively refined by Pia (Pia et al., 2015a, 2016a, 2018; Pia and Casnedi, 2017). The model modifies the classic Sierpinski fractal carpet into a new construction unit, called the intermingled fractal unit (IFU), and combines IFUs with different iteration rules to form an intermingled fractal model (IFM). IFM can be used to predict the heat transfer (Pia and Sanna, 2014a), mechanical properties (Pia et al., 2015b), adsorption (Pia et al., 2016b), and seepage characteristics (Pia, 2016) of porous media. Intuitively, IFM can be viewed as a combination of several different fractal units, enabling it to describe the local features of complex reservoir spaces more accurately. By adjusting the iteration rules and the number of fractal units, the model can flexibly simulate any structure of porous media, including both fractal and non-fractal types (Pia and Sanna, 2014b).

Currently, IFM has attracted widespread attention in various fields (Brun et al., 2018; Casnedi et al., 2020). Based on intermingled fractal theory, Li et al. (2018) performed a rapid evaluation of the permeability of organic-rich shale and further developed an IFU-based spontaneous imbibition model for tight sandstone (Li et al., 2022a), with the model's predictions aligning well with experimental data. Zhang et al. (2018) applied the proposed IFM to simulate the multi-component structure of natural gas hydratebearing sediments and obtain the theoretical solutions for the amount of substance, dissociation rate, and maximal dissociation time of any arbitrary hydrate element in the sediments. Niu et al. (2020) reconstructed the pore structure of hybrid fibrereinforced concrete based on IFUs and demonstrated that, compared to other fractal models, IFM not only has better capabilities in simulating pore size distribution (PSD) but also offers higher fitting accuracy. In summary, the intermingled fractal method can rapidly generate a large number of pores, and based on the generated pore distribution spectrum, it can effectively simulate the physical and mechanical properties of actual porous media. Theoretically, increasing the number of fractal unit types improves the simulation accuracy, but it also raises the computational effort (Zhou et al., 2021). As a result, the number of fractal unit types should be determined according to the complexity of the actual core sample. Previous studies suggest that selecting three to four types of fractal units is generally sufficient to meet accuracy requirements (Li et al., 2018, 2022a).

However, the basic fractal units in existing IFMs are based on the modified Sierpinski fractal carpet (Pia and Sanna, 2013). This means that the pore shapes generated by the model are limited to regular forms (such as square or circular cross-sections), which differ significantly from the complex and irregular pore structures found in actual reservoirs, thereby limiting the model's applicability under real geological conditions. In fact, the geometric shape of the pores has a significant impact on the seepage characteristics, especially in low-permeability or tight rocks. There have been many related studies focused on modeling pore cross-sections using non-circular shapes, such as rectangle (Kim et al., 2023), triangle (Yang et al., 2025), oval (Shi et al., 2019), hexagon (Li et al., 2023), and slit (Afagwu et al., 2024). In addition, some researchers have developed spontaneous imbibition model (Cai et al., 2014) and permeability model (Qiu et al., 2024) based on the assumption of variable cross-sectional pore channels. In these models, geometric factor describing pore shape typically need to be determined indirectly through image analysis or experiments. Also, Liu et al. (2021) theoretically derived a fractal model for shape factor, expressing it as a function of porosity, pore area, and tortuosity fractal dimension. The results show that the model provides an accurate estimation of the shape factor. However, a common limitation of these studies is that the shape factor is often treated as a constant in flow behavior predictions, overlooking the diversity of pore shape characteristics (Wu and Wang, 2020). Similarly. Dong et al. (2021) calculated the average shape factor of pores in various rock samples and incorporated this value into the seepage model for calculation. This approach also has clear limitations. Recently, Qin et al. (2022) revealed the relationship between the shape factor, pore diameter, and Euler number based on a 3D digital core model, and studied the impact of different pore morphologies on permeability. However, this work needs to incorporate numerical simulation results. Therefore, the existing theoretical research in this field remains insufficient. To better describe the complexity of pore morphology in real reservoirs, relevant theoretical models need further refinement and development.

This paper presents a new model for simulating microscopic pore geometry. Specifically, the cross-sectional shape of the pore channels is modeled as fractal units with varying features, and the pore structure is finely reconstructed using the intermingled fractal method. Detailed parameters of each pore (e.g., wetted perimeter, cross-sectional area, and hydraulic diameter) are calculated, and different shape factors are assigned to each pore to establish a relative permeability model based on the IFUs. The model's predictions are then compared with experimental data for validation, followed by an analysis of the influencing factors. This model quantifies the impact of micro-pore geometry on flow, enabling a more accurate depiction of two-phase flow characteristics and the generation of reliable relative permeability curves.

2. The proposal of the novel IFM

2.1. Limitations of traditional IFUs

Fig. 1 illustrates the iterative process of a traditional fractal unit. Each unit starts with a square block, where *i* denotes the iteration count in the figure. In the first iteration, the side length is divided into three equal parts, turning a large square into nine smaller squares, with the center and bottom-left squares removed. In the second iteration, the same operation is applied to the remaining

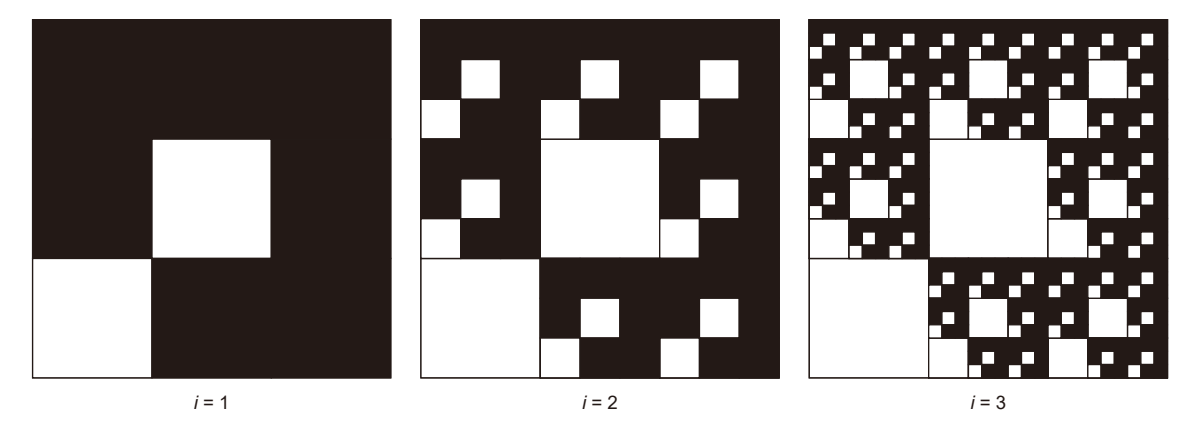


Fig. 1. Iteration process for one traditional fractal unit.

eight smaller squares, continuing indefinitely. The white areas in the figure represent pores, and the black areas denote the matrix. In fact, the number and position of the sub-squares removed can be defined arbitrarily in each iteration. This means that these traditional IFUs are fundamentally modified versions of the Sierpinski carpet.

It is evident that traditional IFUs have clear limitations. First, simulating the pore cross-sectional shape as a square (or its inscribed circle) significantly deviates from the actual shape. Secondly, the merging of the parent pores and the newly generated child pores is not considered as iteration count increases. Specifically, when i=2, it can be observed that the 1st-level pores (defined as the pores generated when i=1, with similar definitions for other levels, i.e., the pores generated in the i-th iteration are defined as i-level pores) come into contact with the 2nd-level pores (corresponding to i=2). At i=3, more interactions between the 1st-level, 2nd-level, and 3rd-level pores occur. Next, we will

further illustrate the merging of parent and child pores through physical characterization experimental results.

A dense sand-conglomerate sample was selected from the Mahu area of the Junggar Basin in China, and high-precision scanning was conducted using the modular automated processing system (MAPS). The FEI-manufactured Helios Nanolab 650 field emission scanning electron microscope was used, with a maximum resolution of 15 nm. MAPS automatically stitches 660 high-resolution small images into a large image, with a total pixel size of approximately $30,000 \times 28,000$ pixels and a field of view of about 2.7 mm \times 2.5 mm, meeting both resolution and research scale requirements. The scanning duration for the sample is 12 h, and the Microsoft HD View plug-in is required for displaying the scanning results.

The sample exhibits a porosity of 12.1% and a permeability of 0.033 mD, collected from a depth of 2644.4 m. Fig. 2 shows the MAPS scanning results, illustrating variations in pore size and edge

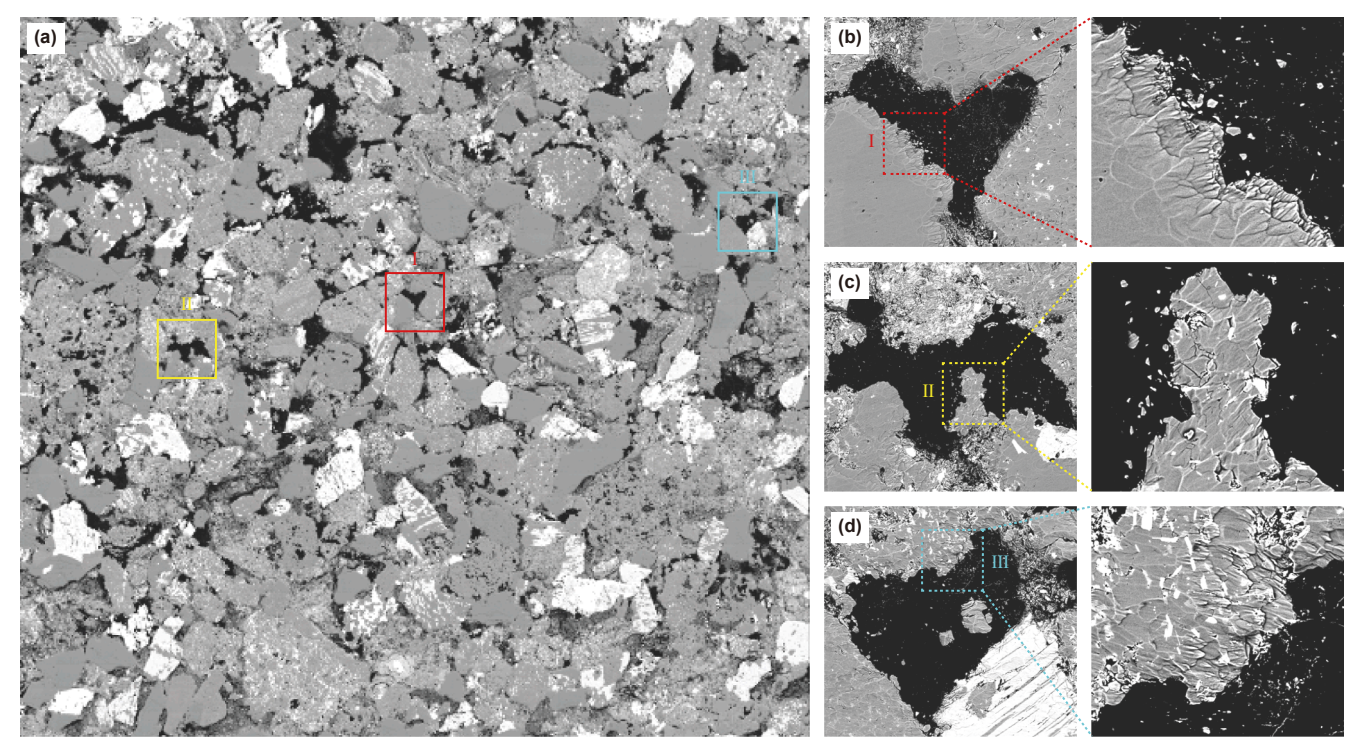


Fig. 2. MAPS scanning image of a conglomerate sample. (a) Overall view. (b) Zoom-in of Zone I. (c) Zoom-in of Zone II. (d) zoom-in of Zone III.

morphology at different resolutions. As the resolution increases, more details gradually emerge, such as larger pore cross-sectional areas and more tortuous and complex edge morphologies. Therefore, it is essential to consider this realistic situation in the pore structure modeling process. In traditional fractal units, however, researchers have not accounted for this and instead treat pores at different levels as completely independent entities, which are then used for flow rate calculations and permeability predictions. This inevitably results in significant computational errors.

2.2. The concept of the new fractal units

Recently, Kong et al. (2023) and Zhao et al. (2024) proposed that rocks consist of numerous solid clusters with unequal diameters, and pores are formed by solid particles surrounding them. This effectively describes the spatial relationship between pores and solid-phase particles in real reservoirs. In this study, we maintain this assumption. Note that in high-pressure geological environments, solid particles are arranged relatively tightly, tending to form a regular hexagonal pattern (with the centers of the solid particles located at the vertices of the hexagon) rather than a square arrangement, which is undercompacted. The simplified model is shown in Fig. 3.

Numerous studies indicate that the distribution of solid particles and pore sizes in porous media follows a fractal pattern (Yu et al., 2014). To construct a pore model that reflects physical realities, we define several distinct fractal units to describe the relationship between pores and particles. Fig. 4 exhibits the iterative processes of four fractal units. Each fractal unit originates from a large solid particle with a circular cross-section. Since no iteration has occurred at this stage, and following the rules for defining pore levels, we classify it as a 0-level solid particle (corresponding to i = 0). Next, taking Unit A as an example, in the first iteration, the large 0-level solid particle splits into seven smaller 1level particles. In the figure, the gray areas represent the solid phase, while the white areas denote the pore phase. It is clear that there are two types of 1st-level pores: six internal pores, formed by three adjacent solid particles (called inner pores, denoted as $P_{\rm in}$ (1)), and six new pores that appear at the edge of the initial 0-level particles (called edge pores, labeled as $P_{\text{out}}(1)$).

In the second iteration, each 1st-level solid particle splits into seven 2nd-level particles following the same iterative rule. Also, six 2nd-level pores are generated inside and at the edges of the 1st-level solid particles (denoted as $P_{\rm in}$ (2) and $P_{\rm out}$ (2), respectively). It should be noted that in some areas, 1st-level pores and 2nd-level pores come into contact and then merge. Specifically, each $P_{\rm in}$ (1) pore merges with three $P_{\rm out}$ (2) pores, forming a larger pore with more winding and intricate edges. Here, we still refer to

it as the 1st-level pore; that is, according to its original designation, and this convention holds for subsequent iterations. Similarly, each $P_{\rm out}$ (1) pore merges with four $P_{\rm out}$ (2) pores to form larger pores. The diameter ratio of solid particles between each level and the sub-level is 3:1. It can be observed that as the iteration count increases, new pores are continuously generated, and a large number of pores merge with each other. When the iteration count reaches four, the constructed porous media becomes highly complex.

To further enhance the ability of the fractal units to simulate real rocks, Units B to D were also introduced in this work. Their iteration rules are similar to those of Unit A, except the black regions represent non-iterative areas. In other words, these regions do not participate in the iteration process and are permanently retained as part of the matrix, without splitting into new secondary solid particles. The new fractal units differ in terms of quantity, size, and iteration parameters. This innovative design allows the pore model to more closely align with the previously mentioned fundamental assumption, thereby improving simulation precision for real reservoirs.

In Fig. 4, $N_{\rm S}$ represents the number of solid particles split into sub-particles in each iteration, with values of $N_{\rm As}=7$, $N_{\rm Bs}=6$, $N_{\rm Cs}=4$, and $N_{\rm Ds}=3$. $N_{\rm n}$ is the number of solid particles that do not participate in the iteration, with values of $N_{\rm An}=0$, $N_{\rm Bn}=1$, $N_{\rm Cn}=3$, and $N_{\rm Dn}=4$. It is evident that, from Unit A to D, the porosity of the fractal units decreases sequentially. These four types of fractal units effectively simulate the multifractal characteristics of real porous media, each exhibiting a symmetric distribution structure. In fact, the distribution of non-iterative solid particles may be asymmetric. However, it is found that this design method has a limited impact on enhancing the simulation capability of the fractal units. On the contrary, it significantly increases the complexity of the model and reduces computational efficiency.

Additionally, Fig. 4 reveals that as the number of iterations increases, the geometric structure of different fractal units becomes increasingly refined and complex at smaller scales. This demonstrates the advantage of the proposed units; that is, they fully utilize self-similarity to represent complex structures that align with physical reality using only a few parameters. Since the basic representative unit in the packing of equal-diameter circular particles is a regular hexagon (as shown in Fig. 3), it is necessary to trim the IFUs into regular hexagons before combining them into an IFM to simulate porous structures (Fig. 5).

To summarize, the design of these fractal units with specialized structures is intended to reflect the observed phenomenon illustrated in Fig. 2. That is, as the resolution or magnification increases, more pore details become visible, such as a slight increase in pore area and a greater winding and tortuosity of the pore edges. Fig. 5 exhibits the changes in the $P_{\rm in}$ (1) pore of Unit A during the

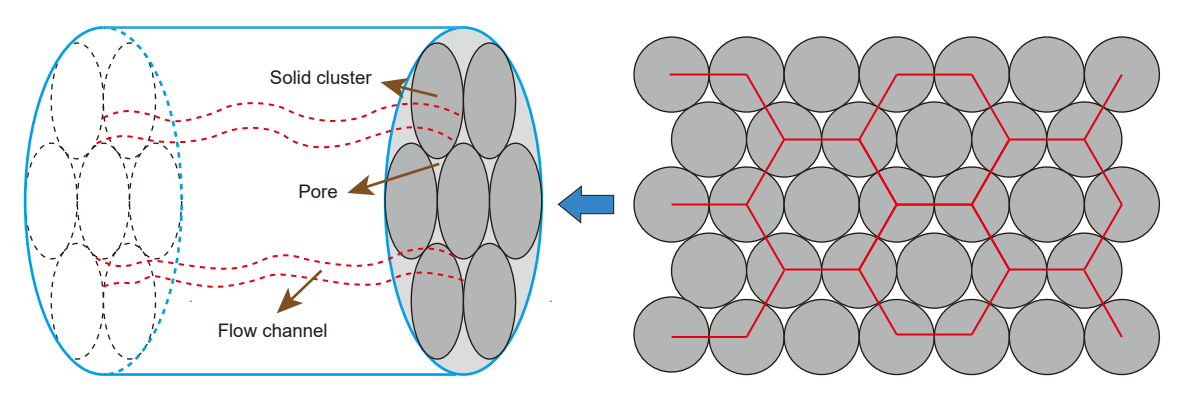


Fig. 3. Schematic diagram of the equivalence rock model.

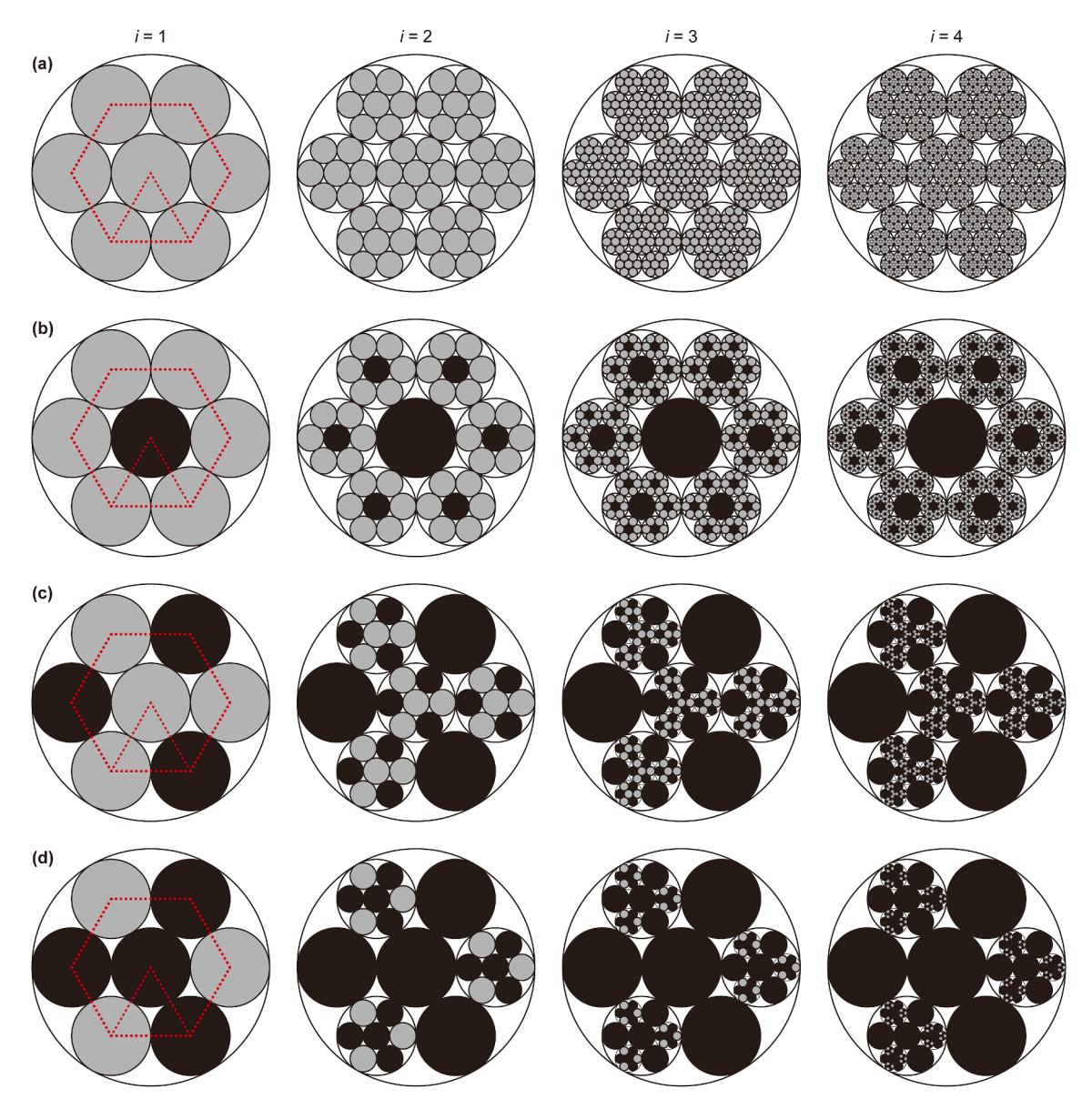


Fig. 4. The Schematic diagram showing the iteration process of new fractal units. (a) Unit A with $N_{As} = 7$ and $N_{An} = 0$, N_s and N_n represent the number of solid particles split from parent solid particles into child solid particles during each iteration and the number of solid particles that do not participate in the iteration, respectively. (b) Unit B with $N_{Bs} = 6$ and $N_{Bn} = 1$. (c) Unit C with $N_{Cs} = 4$ and $N_{Cn} = 3$. (d) Unit D with $N_{Ds} = 3$ and $N_{Dn} = 4$.

iteration process. The figure shows that by the fourth iteration, the growth in pore area becomes relatively stabilized, while the perimeter significantly expands, and the irregularity of the pore shape increases substantially. Obviously, this pattern is consistent with the experimental observation that higher resolution leads to more details.

2.3. Iterative parameters of the novel fractal units

Section 2.2 outlines the conceptual process of the novel IFUs. These IFUs enable efficient reconstruction of the internal structure of complex porous media, allowing for accurate prediction of the flow behavior. This section analyzes the iterative rules for each type of fractal unit. To illustrate the relationship between various fractal iteration parameters, we use Unit A as an example. Given

the similarity ratio of 3:1, the radius of the i-th level solid particle is:

$$r_i = \frac{r_0}{3^{i-1}} \tag{1}$$

where r_0 and r_i are the radii of the 1st-level and the i-th level solid particles, respectively. As shown in Fig. 6, let $S_{\rm in}(i)$ denote the area of a single internal pore enclosed by the i-th level solid particles, and $S_{\rm out}(i)$ represent the area of a single edge pore. Through geometric analysis, the following holds:

$$S_{\text{in}}(i) = \frac{\left(\sqrt{3} - \frac{\pi}{2}\right)r_0^2}{3^{2(i-1)}}$$
 (2-1)

$$S_{\text{out}}(i) = \frac{\left(\frac{5\pi}{6} - \sqrt{3}\right)r_0^2}{32(i-1)} \tag{2-2}$$

Let $L_{\rm in}(i)$ denote the arc length between the surface contact points of adjacent i-th level solid particles (i.e., one edge of the internal pore), with a central angle of 60° . Similarly, define $L_{\rm out}(i)$ as the arc length corresponding to a central angle of 120° (i.e., one edge of the outer pore). Thus, we have:

$$L_{\rm in}(i) = \frac{\pi}{3i} r_0 \tag{3-1}$$

$$L_{\text{out}}(i) = \frac{2\pi}{3i}r_0 \tag{3-2}$$

Due to the symmetric structure of the designed fractal units, representative triangular units can be extracted from the regular hexagonal units, with the area of each triangular unit being one-sixth that of the hexagonal ones. The former retain all the iterative information of the latter and are more compact, allowing for a finer simulation of the local features of actual rocks (see Fig. 7, where the notation Unit A-D is maintained). It should be noted that in each iteration, the newly generated edge pores undergo fusion, which increases the pore area but does not increase the number of pores. Therefore, to simplify the expression, the *i*-th level internal pore is referred to as the *i*-th level pore directly.

For the simplified triangular units, let m represents the total number of iterations. As the iteration progresses, the recursive formula for the area of the 1st-level pore A(1), is derived using mathematical induction, as follows:

$$\begin{cases} A(1)_m = S_{\text{in}}(1), & m = 1 \\ A(1)_m = A(1)_{m-1} + 3 \cdot 4^{m-2} \cdot S_{\text{out}}(m), & m \ge 2 \end{cases}$$
 (4)

In Eq. (4), the subscripts in A (1) $_m$ and A (1) $_{m-1}$ represent the iteration counts. $S_{\rm in}$ (1) and $S_{\rm out}$ (m) refer to the area of the 1st-level internal pore and the area of the m-th level edge pore, respectively. Through the recursive formula, the general term formula can be further derived as shown below:

$$\begin{cases} A(1)_{m} = S_{\text{in}}(1), & m = 1\\ A(1)_{m} = S_{\text{in}}(1) + 3 \cdot \sum_{k=2}^{m} \left(4^{k-2} \cdot S_{\text{out}}(k) \right), & m \ge 2 \end{cases}$$
 (5)

The perimeter of the 1st-level pore P(1) is:

$$\begin{cases} P(1)_{m} = 3L_{\text{in}}(1), & m = 1 \\ P(1)_{m} = 6 \cdot 4^{m-2} \cdot L_{\text{out}}(m), & m \ge 2 \end{cases}$$
 (6)

This can be generalized further. When the total number of iterations is m, the i-th level pore $(i \le m)$ participates in m-i+1 iterations. Therefore, as the iteration progresses, the recursive formula and the general term formula for its area A(i) are given by:

$$\begin{cases} A(i)_{m} = S_{\text{in}}(i), & m = i \\ A(i)_{m} = A(i)_{m-1} + 3 \cdot 4^{m-i-1} \cdot S_{\text{out}}(m), & m \ge i+1 \end{cases}$$
(7-1)

$$\begin{cases} A(i)_{m} = S_{\text{in}}(i), & m = i \\ A(i)_{m} = S_{\text{in}}(i) + 3 \cdot \sum_{k=i+1}^{m} \left(4^{k-i-1} \cdot S_{\text{out}}(k) \right), & m \ge i+1 \end{cases}$$
 (7-2)

The relationship between the perimeter P(i) of the i-th level pore and the iteration number is as follows:

$$\begin{cases}
P(i)_{m} = 3L_{\text{in}}(i), & m = i \\
P(i)_{m} = 6 \cdot 4^{m-i-1} \cdot L_{\text{out}}(m), & m \ge i + 1
\end{cases}$$
(8)

Finally, the number of i-th level pores generated in the i-th iteration, denoted as n_i , is given by Eq. (9):

$$\begin{cases}
 n_i = 1, & i = 1 \\
 n_i = 3 \times 7^{i-2}, & i \ge 2
\end{cases}$$
(9)

Similarly, the fractal iteration parameters for Units B–D can be obtained, as detailed in Appendix Table A1. It can be seen that although the iteration rules for each unit are relatively simple, the derived fractal parameters can be employed to characterize complex porous structures.

3. Modeling for relative permeability

3.1. IFM for absolute permeability

Fluid flow in porous media is usually treated as flow through capillary channels with varying curvatures. The flow rate q in a capillary with a circular cross-section is typically governed by the classic Hagen-Poiseuille law. However, in natural rocks, the flow channels are often non-circular and tortuous. To address this, some early studies have modified the H-P equation to describe flow in non-circular channels (Lewis and Boose, 1995; Mortensen et al., 2005). For example, Pickard (1981) proposed replacing the diameter of the circular tube in the H-P equation with the hydraulic diameter, namely:

$$q = \frac{\pi d_{\rm h}^{\ 4} \Delta p}{128\mu_0 L_0} \tag{10}$$

where $d_{\rm h}$ represents the hydraulic diameter of a channel with an arbitrary cross-sectional shape, Δp is the driving pressure difference, μ_0 is the intrinsic viscosity of the fluid, and L_0 refers to the characteristic length of the channel. Channels with different cross-sectional shapes exhibit distinct flow characteristics, whereas the hydraulic diameter connects flow resistance with the channel's geometry, providing a comprehensive reflection of the impact of the channel shape on flow resistance (Zhao et al., 2021). A larger hydraulic diameter typically corresponds to lower flow resistance. In fact, the hydraulic diameter, as a key parameter in hydraulics, reflects the "effective" flow area in the capillaries and has been extensively used to characterize the hydraulic properties of noncircular cross-sectional channels. The hydraulic diameter is defined as four times the cross-sectional area A divided by the wetted perimeter $P_{\rm c}$, as follows:

$$d_{\rm h} = \frac{4A}{P} \tag{11}$$

It should be emphasized that in various quantitative characterization methods for rock pore size (e.g., mercury injection capillary pressure (MICP) experiments) and qualitative methods (e.g., X-ray computed tomography scanning), the pore structure is typically represented using a capillary or ball-and-stick model with a regular circular cross-section. As a result, the measured pore size is actually the diameter of the equivalent circular cross-section or spherical shape (Dong et al., 2021). The introduction of the equivalent circular diameter aims to simplify flow analysis by

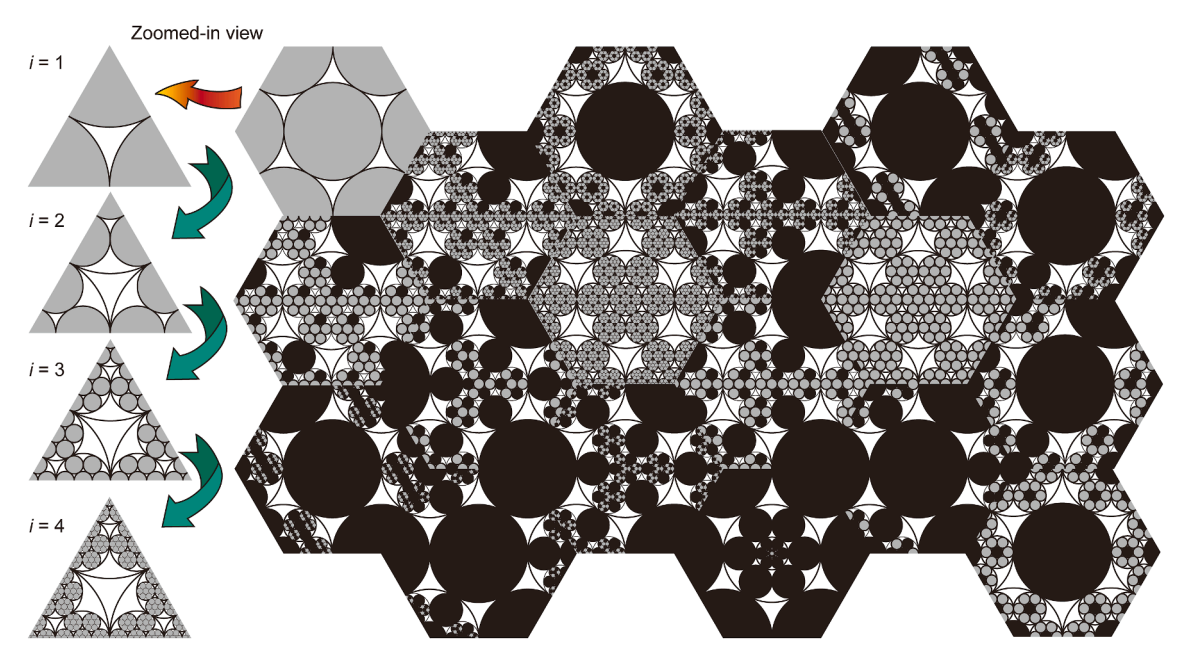


Fig. 5. Schematic diagram of the intermingled fractal model and zoomed-in view.

converting complex non-circular channels into a circular one, as determined by the following:

$$d_{e} = 2\sqrt{\frac{A}{\pi}} \tag{12}$$

where A represents the area of the non-circular cross-section, and $d_{\rm e}$ is the equivalent circular diameter. Since the equivalent circular diameter does not involve the concept of the wetted perimeter, directly substituting it into the H-P equation for flow calculation in a single capillary would inevitably lead to an overestimation of the flow rate compared to the actual situation. This is due to the fact that, for a fixed flow cross-sectional area, the wetted perimeter of a circular cross-section is minimal, and its flow capacity is maximal. In other words, using the equivalent circular diameter for flow calculation is identical to directly selecting the hydraulically optimal cross-section, which does not reflect the practical reality. This further supports the reasonableness of using the hydraulic diameter in Eq. (10). Based on Eqs. (11) and (12), the relationship between the hydraulic diameter and the equivalent circular diameter is given by:

$$d_{\rm e} = \sqrt{\frac{Pd_{\rm h}}{\pi}} \tag{13}$$

Columns 3 and 4 in Appendix Table A1 display the iterative patterns of the area and perimeter of the i-th level pore in different types of fractal units, and Column 5 presents the hydraulic diameter calculated using Eq. (11). The validity of applying the hydraulic diameter in describing flow behavior is further discussed in Section 4.1.

In addition, numerous studies have demonstrated that the boundary layer effect in tight reservoirs cannot be ignored (Wang et al., 2020). Under low-speed and low-pressure conditions, the boundary layer thickness can account for more than 50% of the entire flow space and may even completely block the throat,

leading to non-linear flow characteristics in the microcapillaries (Li et al., 2011). However, investigating the quantitative relationship between the thickness of boundary layer and various influencing factors remains highly challenging. As a result, nearly all formulas describing boundary layer thickness include empirical constants (Tian et al., 2015; Xiong et al., 2017). The boundary layer is a non-flow (or difficult-to-flow) region caused by the solid-liquid effect. Specifically, near the pore wall, the attraction between the solid surface and fluid molecules significantly increases the fluid viscosity. In light of this, to avoid introducing additional empirical coefficients into the IFM, this section considers the non-uniform distribution of fluid viscosity as a replacement for the boundary layer effect.

In our previous study, a flow rate expression for a single capillary with fractal distribution characteristics was proposed, considering the variation in fluid viscosity (Zhou et al., 2025). Here, we replace the capillary radius in the original expression with the hydraulic diameter, as follows:

$$q(d_{\rm h}) = \frac{\pi d_{\rm h}^{D_{\rm T}+3} \Delta p}{32\mu_0 L_0^{D_{\rm T}} (D_{\rm T}+3)(D_{\rm T}+4)} \tag{14}$$

where $D_{\rm T}$ represents the average tortuosity fractal dimension, given by Yu et al. (2014):

$$D_{\mathrm{T}} = 1 + \frac{\ln \tau_{\mathrm{av}}}{\ln \frac{L_0}{d_{\mathrm{av}}}} \tag{15}$$

In Eq. (15), the average capillary diameter in the original equation is replaced with the average hydraulic diameter d_{av} . τ_{av} denotes the average tortuosity. To determine the parameters in Eq. (15), a cubic representative elementary volume (REV) with a characteristic length of L_0 is used for analysis. Assume that a large number of fractal units, following different iteration rules, are distributed on a two-dimensional plane of the REV. Let N_A , N_B , N_C ,

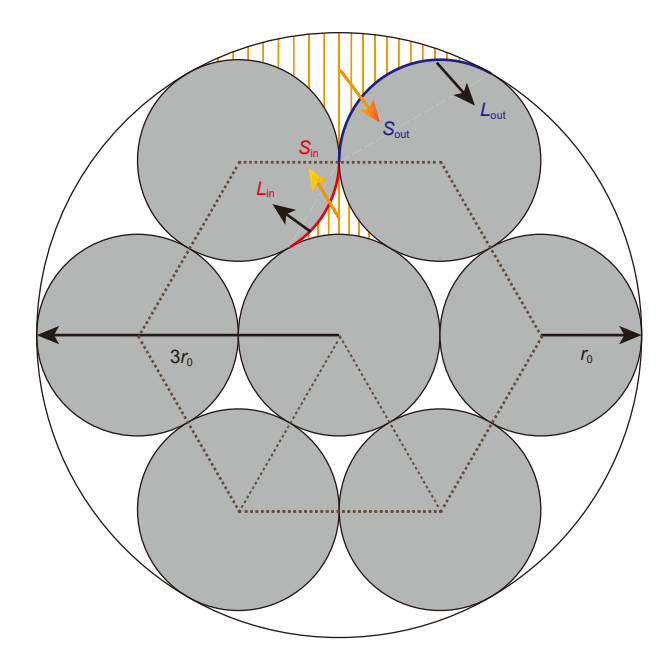


Fig. 6. Fractal parameters of Unit A.

and N_D represent the number of different types of units, and define m_A , m_B , m_C , and m_D as the total number of iterations for each unit. Then, the total pore area in the REV can be calculated as:

$$L_0 = \sqrt{\frac{\sum\limits_{J \in \Omega} \sum\limits_{i=1}^{m_J} \left(N_J \cdot n_{i,J} \cdot A(i)_{m_J} \right)}{\phi}}$$
(18)

Note that L_0 and A_t do not represent the actual edge length and cross-sectional area of the sample. Next, to calculate the tortuosity fractal dimensions $D_{T,\tilde{A}}$ and $D_{T,D}$ for each fractal unit, Unit A remains employed as an example for clarity. As described in Section 2.3, the edge length of Unit A is $2r_{0,A}$, and its area can be determined as:

$$S_{\rm A} = \sqrt{3}r_{\rm 0.A}^2$$
 (19)

After m_A iterations, the porosity of Unit A, ϕ_A , is given by:

$$\phi_{A} = \frac{\sum_{i=1}^{m_{A}} \left(n_{i,A} \cdot A(i)_{m_{A}} \right)}{S_{\Delta}}$$
 (20)

The average hydraulic diameter of the cross sections of the capillaries generated by Unit A, $d_{av,A}$, is calculated as follows:

$$d_{\text{av,A}} = \frac{\sum_{i=1}^{m_{\text{A}}} \left(n_{i,\text{A}} \cdot d_{\text{h}}(i)_{m_{\text{A}}} \right)}{\sum_{i=1}^{m_{\text{A}}} n_{i,\text{A}}}$$
(21)

where $d_{\rm h}(i)_{m_{\rm A}}$ represents the hydraulic diameter of the *i*-th level

$$A_{p} = N_{A} \sum_{i=1}^{m_{A}} \left(n_{i,A} \cdot A(i)_{m_{A}} \right) + N_{B} \sum_{i=1}^{m_{B}} \left(n_{i,B} \cdot A(i)_{m_{B}} \right) + N_{C} \sum_{i=1}^{m_{C}} \left(n_{i,C} \cdot A(i)_{m_{C}} \right) + N_{D} \sum_{i=1}^{m_{D}} \left(n_{i,D} \cdot A(i)_{m_{D}} \right) = \sum_{J \in \Omega} \sum_{i=1}^{m_{J}} \left(N_{J} \cdot n_{i,J} \cdot A(i)_{m_{J}} \right)$$
(16)

where A_p represents the total area of the generated pores, $\Omega = \{A, B, C, D\}$. $n_{i,j}$ is the number of i-th level pores generated by each fractal unit, and $A(i)_{mj}$ denotes the area of the i-th level pores at a total of m_j iterations. The values of these parameters in different IFUs are provided in Appendix Table A1. Thus, the cross-sectional area of the REV is expressed as:

$$A_{t} = L_{0}^{2} = \frac{A_{p}}{\phi} = \frac{\sum_{j \in \Omega} \sum_{i=1}^{m_{j}} \left(N_{J} \cdot n_{i,J} \cdot A(i)_{m_{j}} \right)}{\phi}$$

$$\tag{17}$$

where ϕ is the porosity of the rock sample. The edge length of the REV is given by:

pore in Unit A, with the specific expression provided in Appendix Table A1. Regarding the calculation of the average tortuosity $\tau_{\rm aw}$, Yu and Li (2004) proposed an analytical model for the tortuosity-porosity relationship of porous media composed of square particles. Subsequently, Yun et al. (2006) further developed the equation applicable to circular particles as follows:

$$\tau_{av} = 1 - \frac{\phi}{2} + \frac{\sqrt{1 - \phi}}{4} + \frac{\left(\phi + 1 + \sqrt{1 - \phi}\right) \cdot \sqrt{9 - 5\phi - 8\sqrt{1 - \phi}}}{8\phi}$$
(22)

Substituting Eq. (20) into Eq. (22) yields the average tortuosity of Unit A, $\tau_{\text{av,A}}$. Then, substituting Eqs. (18) and (21) into Eq. (15) determines the average tortuosity fractal dimension of Unit A, denoted as $D_{\text{T,A}}$. Similarly, $D_{\text{T,B}}$ to $D_{\text{T,D}}$ can be calculated using the same method.

Therefore, based on Eq. (14), the total flow rate Q passing through the cross-section of the REV is obtained by summing the individual capillary flow rates:

$$Q = \frac{\pi \Delta p}{32\mu_{0}} \begin{pmatrix} N_{A} \sum_{i=1}^{m_{A}} \left(\frac{n_{i,A} \cdot d_{h}^{D_{T,A}+3}(i)_{m_{A}}}{L_{0}^{D_{T,A}}(D_{T,A}+3) \left(D_{T,A}+4\right)} \right) + N_{B} \sum_{i=1}^{m_{B}} \left(\frac{n_{i,B} \cdot d_{h}^{D_{T,B}+3}(i)_{m_{B}}}{L_{0}^{D_{T,B}+3}(D_{T,B}+4)} \right) + \\ N_{C} \sum_{i=1}^{m_{C}} \left(\frac{n_{i,C} \cdot d_{h}^{D_{T,C}+3}(i)_{m_{C}}}{L_{0}^{D_{T,C}}(D_{T,C}+3) \left(D_{T,C}+4\right)} \right) + N_{D} \sum_{i=1}^{m_{D}} \left(\frac{n_{i,D} \cdot d_{h}^{D_{T,D}+3}(i)_{m_{D}}}{L_{0}^{D_{T,D}+3}(D_{T,D}+4)} \right) \end{pmatrix} = \frac{\pi \Delta p}{32\mu_{0}} \sum_{j \in \Omega} \sum_{i=1}^{m_{J}} \left(\frac{N_{J} \cdot n_{i,J} \cdot d_{h}^{D_{T,J}+3}(i)_{m_{J}}}{L_{0}^{D_{T,J}+3}(D_{T,J}+4)} \right)$$

$$(23)$$

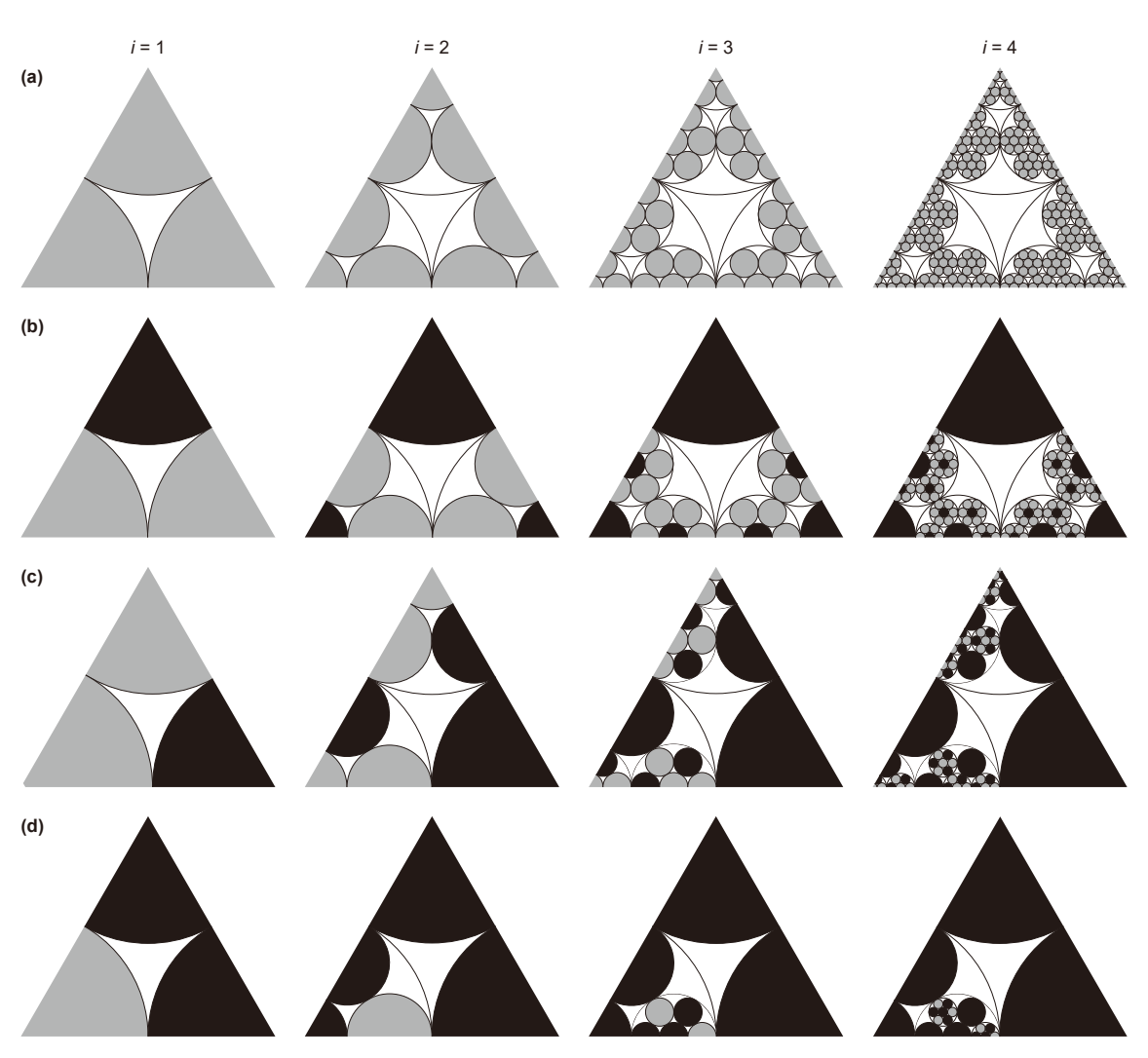


Fig. 7. Iterative process of four representative fractal units. (a) Unit A. (b) Unit B. (c) Unit C. (d) Unit D.

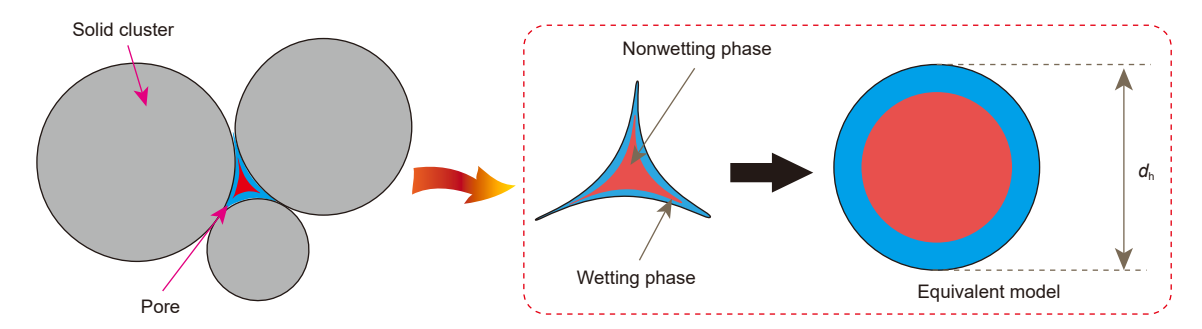


Fig. 8. Schematic diagram of the pore structure.

Finally, by comparing with Darcy's law, the intermingled fractal expression for the absolute permeability K_a is derived as follows:

$$K_{a} = \frac{\pi}{32A_{t}} \sum_{J \in \Omega} \sum_{i=1}^{m_{J}} \left(\frac{N_{J} \cdot n_{i,J} \cdot d_{h}^{D_{\tau_{J}} + 3}(i)_{m_{J}}}{L_{0}^{D_{\tau_{J}} - 1}(D_{T,J} + 3)(D_{T,J} + 4)} \right)$$
(24)

Eq. (24) establishes the quantitative relationship between the absolute permeability, pore hydraulic diameter, tortuosity fractal dimension, porosity, and the fractal parameters of dense porous media.

3.2. IFM for relative permeability

Consider an REV composed of a bundle of curved capillaries, where the hydraulic radii distribution follows a multifractal characteristic. Assume that two-phase fluids flowing through the capillaries adhere to the "annular flow" model (Su et al., 2021; Yang et al., 2024; Zhao et al., 2024). The assumptions are as follows: (a) Each capillary is partially filled with both wetting and non-wetting phase fluids, with the non-wetting phase occupying the center and the wetting phase flowing along the wall. The two-phase flow structure in a single capillary is shown in Fig. 8; (b) Both phases are Newtonian fluids and exhibit laminar flow; (c) The two-phase fluids do not interact, and their viscosities are independent; (d) The change in wettability is neglected. Based on these assumptions, the flow rate through a capillary is expressed in an extended form of Eq. (14):

$$q_{\rm W} = \frac{\pi d_{\rm h,w}^{D_{\rm T}+3} \Delta p}{32\mu_{\rm 0,w} L_{\rm 0}^{D_{\rm T,w}} (D_{\rm T,w}+3) (D_{\rm T,w}+4)} \tag{25-1}$$

$$q_{\text{nw}} = \frac{\pi d_{\text{h,nw}}^{D_{\text{T}}+3} \Delta p}{32\mu_{0,\text{nw}} L_0^{D_{\text{T,nw}}} \left(D_{\text{T,nw}} + 3\right) \left(D_{\text{T,nw}} + 4\right)}$$
(25-2)

The subscripts "w" and "nw" represent the wetting and nonwetting phase fluids, respectively. The hydraulic diameters $d_{h,w}$

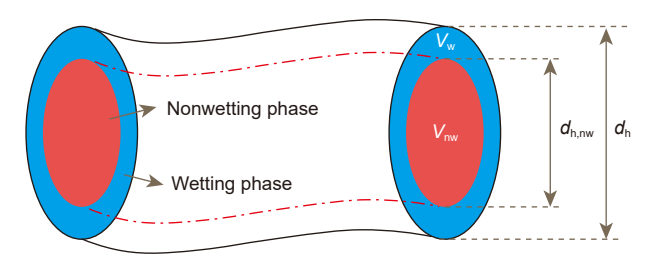


Fig. 9. Schematic diagram of the two-phase flow structure.

and $d_{h,nw}$, corresponding to the wetting and non-wetting phases, respectively, are illustrated in Fig. 9. The figure shows a schematic of the cross section of a capillary tube partially filled with wetting and non-wetting phase. It is assumed that the saturation of the wetting phase is uniform across all capillaries (Qiao et al., 2022), and that the tortuosity of the paths traversed by both phases is approximately equal to that of single-phase flow, i.e., $D_T = D_{T,nw}$ (Yu et al., 2003). Thus, the following can be derived:

$$S_{\text{nw}} = \frac{V_{\text{nw}}}{V_{\text{p}}} = \left(\frac{d_{\text{h,nw}}}{d_{\text{h}}}\right)^2 = 1 - S_{\text{w}}$$
 (26)

where $S_{\rm w}$ and $S_{\rm nw}$ represent the saturations of the wetting and non-wetting phases, respectively. $V_{\rm nw}$ is the volume occupied by non-wetting phase, and $V_{\rm p}$ is the pore volume. Thus, the hydraulic diameter of the non-wetting phase is expressed as:

$$d_{\text{h nw}} = d_{\text{h}} \sqrt{1 - S_{\text{w}}} \tag{27}$$

The hydraulic diameter of the wetting phase can be derived from the occupied annular area and the wetted perimeter as. Specifically, by substituting Eq. (27) into Eq. (11), the following expression is obtained:

$$d_{h,w} = \frac{4\left(\frac{\pi}{4}\left(d_h^2 - d_{h,nw}^2\right)\right)}{\pi d_h} = d_h S_w$$
 (28)

Then, based on Eq. (25), the total flow rate of the wetting and non-wetting phase fluids through the cross-section of the REV can be written as:

$$Q_{w} = \frac{\pi \Delta p}{32\mu_{0,w}} \sum_{I=\Omega} \sum_{i=1}^{m_{J}} \left(\frac{N_{J} \cdot n_{i,J} \cdot d_{h,w}^{D_{T,J}+3}(i)_{m_{J}}}{L_{0}^{D_{T,J}}(D_{T,J}+3)(D_{T,J}+4)} \right)$$
(29-1)

$$Q_{\text{nw}} = \frac{\pi \Delta p}{32\mu_{0,\text{nw}}} \sum_{J \in \Omega} \sum_{i=1}^{m_J} \left(\frac{N_J \cdot n_{i,J} \cdot d_{\text{h,nw}}^{D_{\text{T},J}+3}(i)_{m_J}}{L_0^{D_{\text{T},J}} (D_{\text{T},J}+3) (D_{\text{T},J}+4)} \right)$$
(29-2)

By applying Darcy's extended law to the two-phase flow process, the phase permeability can be obtained as:

$$K_{W} = \frac{Q_{W}\mu_{0,W}L_{0}}{A_{t}\Delta p} = \frac{\pi}{32A_{t}} \sum_{J \in \Omega} \sum_{i=1}^{m_{J}} \left(\frac{N_{J} \cdot n_{i,J} \cdot d_{h,W}^{D_{T,J}+3}(i)_{m_{J}}}{L_{0}^{D_{T,J}-1} \left(D_{T,J}+3\right) \left(D_{T,J}+4\right)} \right)$$
(30-1)

$$K_{\text{nw}} = \frac{Q_{\text{nw}}\mu_{0,\text{nw}}L_0}{A_t\Delta p} = \frac{\pi}{32A_t} \sum_{J \in \Omega} \sum_{i=1}^{m_J} \left(\frac{N_J \cdot n_{i,J} \cdot d_{\text{h,nw}}^{D_{\text{T},J}+3}(i)_{m_J}}{L_0^{D_{\text{T},J}-1} \left(D_{\text{T},J}+3\right) \left(D_{\text{T},J}+4\right)} \right)$$
(30-2)

where $K_{\rm w}$ and $K_{\rm nw}$ are the phase permeabilities of the wetting phase and the non-wetting phase fluids, respectively. Based on the definition of relative permeability, combining Eqs. (24) and (30) yields:

$$K_{\text{rw}} = \frac{K_{\text{w}}}{K_{\text{a}}} = \frac{\sum_{J \in \Omega} \sum_{i=1}^{m_J} \left(\frac{N_J \cdot n_{i,J} \cdot d_{\text{h,w}}^{D_{\text{T},J}+3}(i)_{m_J}}{L_0^{D_{\text{T},J}-1}(D_{\text{T},J}+3)(D_{\text{T},J}+4)} \right)}{\sum_{J \in \Omega} \sum_{i=1}^{m_J} \left(\frac{N_J \cdot n_{i,J} \cdot d_{\text{h}}^{D_{\text{T},J}+3}(i)_{m_J}}{L_0^{D_{\text{T},J}+3}(D_{\text{T},J}+4)} \right)}$$
(31-1)

$$K_{\text{rnw}} = \frac{K_{\text{nw}}}{K_{\text{a}}} = \frac{\sum_{J \in \Omega} \sum_{i=1}^{m_J} \left(\frac{N_J \cdot n_{iJ} \cdot d_{\text{h,nw}}^{D_{\text{T}J}+3}(i)_{m_J}}{L_0^{D_{\text{T}J}-1} (D_{\text{T}J}+3) (D_{\text{T}J}+4)} \right)}{\sum_{J \in \Omega} \sum_{i=1}^{m_J} \left(\frac{N_J \cdot n_{iJ} \cdot d_{\text{h}}^{D_{\text{T}J}+3}(i)_{m_J}}{L_0^{D_{\text{T}J}+3} (D_{\text{T}J}+4)} \right)}$$
(31-2)

where K_{rw} and K_{rnw} represent the relative permeabilities of the wetting and non-wetting phase fluids, respectively. Finally, by substituting Eqs. (27) and (28) into Eq. (31), and expressing the relative permeability as a function of the wetting phase saturation, as follows:

$$K_{\text{TW}} = \frac{\sum_{J \in \Omega} \sum_{i=1}^{m_J} \left(\frac{N_J \cdot n_{iJ} \cdot (d_h S_w)^{D_{\text{T}J} + 3}(i)_{m_J}}{L_0^{D_{\text{T}J} - 1}(D_{\text{T}J} + 3)(D_{\text{T}J} + 4)} \right)}{\sum_{J \in \Omega} \sum_{i=1}^{m_J} \left(\frac{N_J \cdot n_{iJ} \cdot d_h^{D_{\text{T}J} + 3}(i)_{m_J}}{L_0^{D_{\text{T}J} - 1}(D_{\text{T}J} + 3)(D_{\text{T}J} + 4)} \right)}$$
(32-1)

$$K_{\text{TDW}} = \frac{\sum_{J \in \Omega} \sum_{i=1}^{m_J} \left(\frac{N_J \cdot n_{iJ} \cdot \left(d_h \sqrt{1 - S_w} \right)^{D_{\text{T}J} + 3} (i)_{m_J}}{l_0^{D_{\text{T}J} - 1} \left(D_{\text{T}J} + 3 \right) \left(D_{\text{T}J} + 4 \right)} \right)}{\sum_{J \in \Omega} \sum_{i=1}^{m_J} \left(\frac{N_J \cdot n_{iJ} \cdot d_h^{D_{\text{T}J} + 3} (i)_{m_J}}{l_0^{D_{\text{T}J} - 1} \left(D_{\text{T}J} + 3 \right) \left(D_{\text{T}J} + 4 \right)} \right)}$$
(32-2)

Eq. (32) establishes a quantitative relationship between the pore hydraulic diameter, tortuosity fractal dimension, porosity, fractal iterative parameters of the IFM, and the relative permeabilities. It contains no empirical constants, and each parameter has a clear physical interpretation.

3.3. Computational process

The steps for calculating relative permeability using the proposed IFM are as follows:

- 1) Measure the sample's physical properties, including porosity, permeability, and PSD curve. Convert the PSD curve to a cumulative pore size distribution (CPSD) curve to facilitate the reconstruction of the pore structure in the subsequent analysis.
- 2) Adjust the fractal parameters of the model to match the generated CPSD curve with the measured curve as closely as possible, and then record the IFM parameters. For a detailed description of using IFM to rebuild the actual pore structure, please refer to Pia et al. (2015a, 2016a, 2018). As mentioned in Section 3.1, various characterization methods typically express pore size as an equivalent circular diameter. Thus, Eq. (13) is utilized to convert the generated hydraulic diameter to the equivalent circular diameter and fit it with the experimental data.

- 3) Find the side length of REV, porosity, average tortuosity, and average hydraulic diameter for each fractal unit using Eqs. (18) and (20)–(22), respectively, then determine the average tortuosity fractal dimension by Eq. (15).
- 4) Finally, calculate the relative permeability using Eq. (32).

4. Results and discussion

This section validates the effectiveness of the proposed models, which is divided into three parts: first, the validation of the absolute permeability model, which establishes the foundation for subsequent research; second, the validation of the relative permeability model; third, the validation of the generated shape factor. In addition, the impact of different parameters on the seepage characteristics of tight reservoirs is also examined.

4.1. Model validation

4.1.1. Absolute permeability

Four representative tight sand-conglomerate samples from the Karamay Formation, Mahu Sag, Junggar Basin, were selected for permeability testing experiments. The flow rate was controlled at approximately 0.05 mL/min, and each sample was measured three times, with the average value used. The four samples exhibit varying physical properties, with porosity ranging from 6.3% to 14.3% and permeability from 0.081 to 7.921mD. Based on the measured results, the proposed absolute permeability model (Eq. (24)) was validated and compared with the predictions of the classic IFM by Pia and Sanna (2014b). Table 1 presents the basic physical properties of the samples and compares the calculations of the new model with those of the Pia and Sanna model.

Table 1 shows that the predicted values from the new model exhibit good consistency with the measured ones, with relative errors within 10%. This indicates that Eq. (24) is effective and reliable in simulating real porous media and calculating absolute permeability. In contrast, as the sample permeability decreases, the calculation error of the Pia model increases, thereby demonstrating its limitations. Also, it was found that the predictions of the Pia model are consistently higher than the experimental ones. In our previous research, this phenomenon was attributed to newly generated fissures caused by excessively high pressure during the MICP experiments (Zhou et al., 2021). Furthermore, in this study, we believe this issue is related to the neglect of pore geometry in traditional IFMs. As discussed in Section 3.1, traditional models use the equivalent circular diameter for flow calculations, which equates to selecting the hydraulically optimal cross-section, thus inevitably overestimating permeability. In other words, as sample density increases, the pore throat geometry becomes more complex, and the deviation of the crosssectional shape from circularity intensifies. This results in a gradual decline in the prediction accuracy of traditional models, which may, in some cases, lead to complete failure. This further

 Table 1

 Comparison of measured and calculated values for permeability.

			Measured	New model		Pia and Sanna model		
No.		%	permeability, mD	Model prediction, mD	Relative error, %	Model prediction, mD	Relative error, %	
1		14.3	7.921	7.682	3.02	9.114	15.06	
2		10.1	1.457	1.462	0.34	1.727	18.53	
3		9.5	0.233	0.215	7.73	0.313	34.33	
4		6.3	0.081	0.088	8.64	0.119	46.91	

Table 2 Physical property analysis results of core samples obtained by Wang et al. (2019).

Sample No.	Porosity, %	permea	Maximum pore radius, µm	Minimum pore radius, nm	Median pore radius, µm	Relative permeability experi ment
145H	18.278	24.44	7.828	2.7	1.791	Gas-oil
192H	12.325	0.60	14.159	2.7	0.558	Gas-oil

supports the reasonableness of using the hydraulic diameter in flow calculations.

4.1.2. Relative permeability

To validate the relative permeability model (Eq. (32)), the calculation results were compared with the experimental data from Wang et al. (2019) for analysis. Consider that the heterogeneity of the pore structure significantly affects the relative permeability curve, leading to variations in the two-phase coexistence region across different samples. To eliminate the impact of these differences, the wetting phase saturation should be standardized when the saturation of irreducible wetting-phase and residual non-wetting-phase exist, i.e., by normalizing it to the [0,1] range (Wang et al., 2019, 2023). This ensures that model predictions and measured data are compared within the same range, thereby enhancing the scientific rigor and accuracy of the comparison (Xu et al., 2013). Table 2 presents the basic physical property parameters of two typical carbonate rock samples reported by Wang et al. (2019).

First, the published capillary pressure curves for two samples were converted into cumulative PSD curves, with pore size calculated using the classical Laplace-Young equation. The surface tension of mercury (σ) is 0.48 N/m, and the contact angle between mercury and air is 140°. Next, the IFM parameters are adjusted to ensure that the CPSD curve generated by the model closely matches the experimental curve (Fig. 10). Table 3 lists the input and output parameters of the IFM. Once the model parameters are determined, the flow behavior within the porous media can then be simulated.

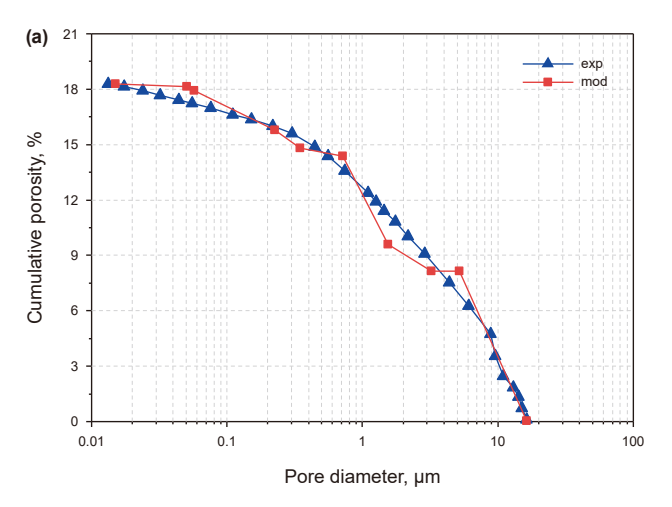
Subsequently, the relative permeability of the wetting and non-wetting phases was calculated under different normalized wetting phase saturation (S_{wn}), and the results were compared with experimental data (Fig. 11). Based on the measured curves for these two samples, Wang et al. (2019) have discussed the limitations of using four classic models (such as Purcell, Burdine, Brooks-

Table 3
Representative input and output parameters of the IFM.

Sample	Unit type	Input parameters		Output parameters						
No.		N	m	r ₀ , μm	$ au_{av}$	d _{av} , μm	D_{T}	$A_{\rm p}$, $\mu{ m m}^2$	A _t , μm ²	L ₀ , μm
145H	Unit A	1	2	21.5	1.88	3.45	1.12	7.7×10^{4}	4.2×10^5	647.6
	Unit B	1.6×10^3	3	6.9	1.81	0.41	1.08			
	Unit C	5×10^{4}	3	1.0	1.90	0.07	1.07			
	Unit D	3.5×10^{6}	2	0.1	2.66	0.02	1.09			
192H	Unit A	1	2	38.0	1.88	6.09	1.13	9.2×10^{4}	7.5×10^{5}	866.1
	Unit B	250	3	12.0	1.81	0.72	1.08			
	Unit C	1×10^5	3	1.0	1.90	0.07	1.07			
	Unit D	8×10^6	2	0.1	2.66	0.02	1.09			

Corey, and Corey models) for predicting relative permeability. In this section, we further introduced several other classic fractal relative permeability models for comparative analysis, including the models by Wang et al. (2019), Xu et al. (2013) and Yu et al. (2003). The results show that, compared to other fractal approaches, the newly developed model demonstrates better agreement with experimental values and improved prediction accuracy. To quantitatively evaluate the predictive ability of each model, the correlation coefficients R^2 between the predictions and experimental results were calculated, as shown in Table 4.

Overall, the new model exhibits the highest performance in predicting the relative permeability curves, with correlation coefficients approaching 1. Wang et al. (2019) model also demonstrates high accuracy in predicting relative permeability, with correlation coefficients for both the wetting and non-wetting phases exceeding 0.99. This is expected, as the model was specifically developed based on mentioned experimental data, making it highly adaptable. Yu et al. (2003) model, a classic fractal model based on the "annular flow" assumption, performs well in predicting non-wetting phase relative permeability but has limitations in predicting the flow capacity of the wetting phase. This is because the model adopts an equivalent circular diameter instead of the hydraulic diameter when deriving the relationship between the flow diameter of the wetting phase and fluid saturation. This method inevitably results in an overestimation of K_{rw} while simultaneously underestimating K_{rnw} . Additionally, the curve exhibits symmetry at $S_{wn} = 0.5$ (i.e., the value of isotonic point saturation is 0.5), reflecting neutral wetting characteristics, which in turn contradicts the model's assumptions. In contrast, Xu et al. (2013) model shows the largest deviation from actual results in



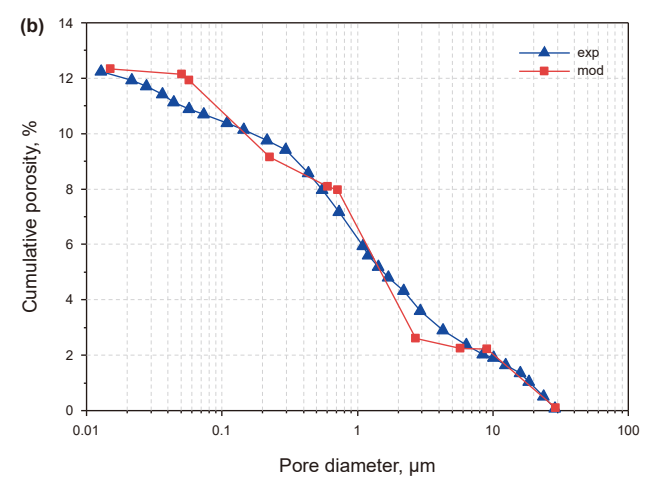


Fig. 10. Comparison of cumulative curve of pore size between the IFU model and experimental data. (a) Sample 145H. (b) Sample 192H.

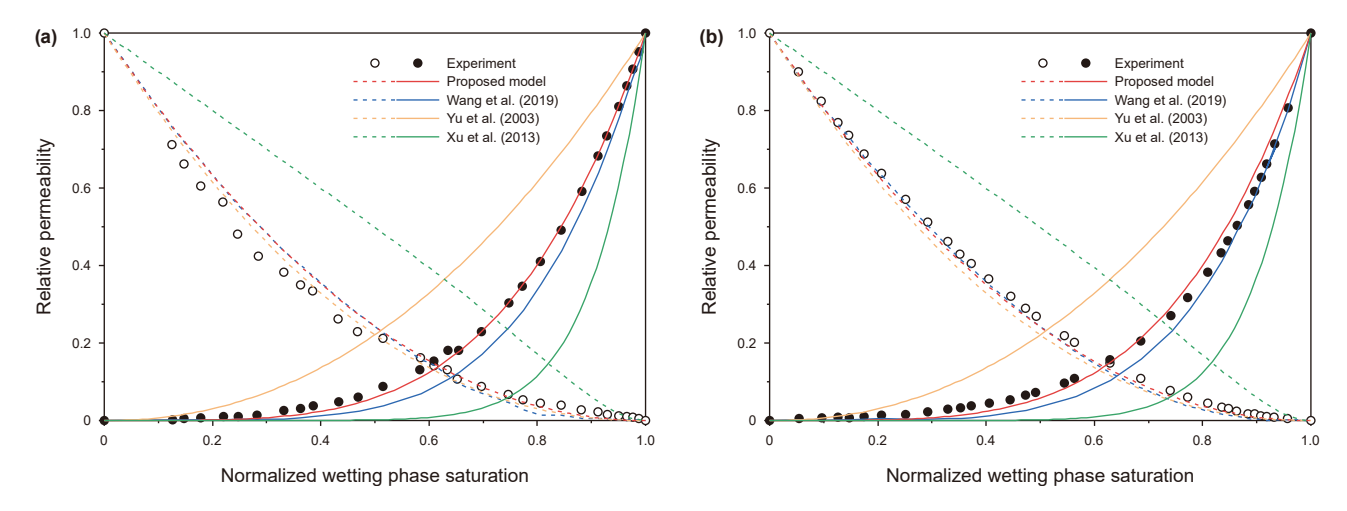


Fig. 11. The predicted relative permeability using different models and compared with experimental results. (a) Sample 145H. (b) Sample 192H.

Table 4Correlation coefficients between predictions from different models and experimental data.

Model	Correlation	Correlation coefficients R ²						
	145H		192H					
	K _{rnw}	K _{rw}	K _{rnw}	K _{rw}				
IFM	0.9965	0.9998	0.9998	0.9986				
Wang et al. (2019)	0.9918	0.9962	0.9996	0.9977				
Yu et al. (2003)	0.9978	0.9743	0.9989	0.9688				
Xu et al. (2013)	0.9407	0.9518	0.9687	0.9483				

predicting relative permeability. This is due to the fact that the model is based on the "critical capillary radius" assumption, suggesting that at a certain driving pressure, the non-wetting fluid occupies all pores larger than the critical capillary radius ($r_{\rm c}$). Specifically, the wetting phase is distributed in capillaries with a radius smaller than $r_{\rm c}$, while those with a radius larger than $r_{\rm c}$ are fully saturated with non-wetting fluid. However, this assumption is unable to fully capture the actual flow behavior of the two-phase and deviates from reality, resulting in significant calculation errors.

4.1.3. Shape factor

Benavente et al. (2002) defined the shape factor δ as the ratio of the hydraulic diameter (d_h) of an irregular cross-section to its equivalent circular diameter (d_e) , as follows:

$$\delta = \frac{d_{\rm h}}{d_{\rm e}} \tag{33}$$

The value of δ typically ranges from 0 to 1, representing the extent to which an irregular cross-section deviates from a circle. The more irregular the cross-sectional morphology, the smaller the δ value becomes. Specifically, the δ values for circular, square, and equilateral triangular cross-sections are 1, 0.886, and 0.778, respectively.

Before validating the pore shape factor generated by the IFM, it is crucial to analyze the evolution of the hydraulic diameter of an individual pore with respect to the number of iterations. Fig. 12 illustrates the variation in geometric parameters of 1st-level pores generated by Unit A and B as the iteration count increases. In fact, Fig. 12 quantitatively represents the enlarged section of Fig. 5, and this pattern holds for other fractal units and pores of all levels. It can be observed that the pore area increases rapidly in the early stages, and then gradually stabilizes. This is because once the

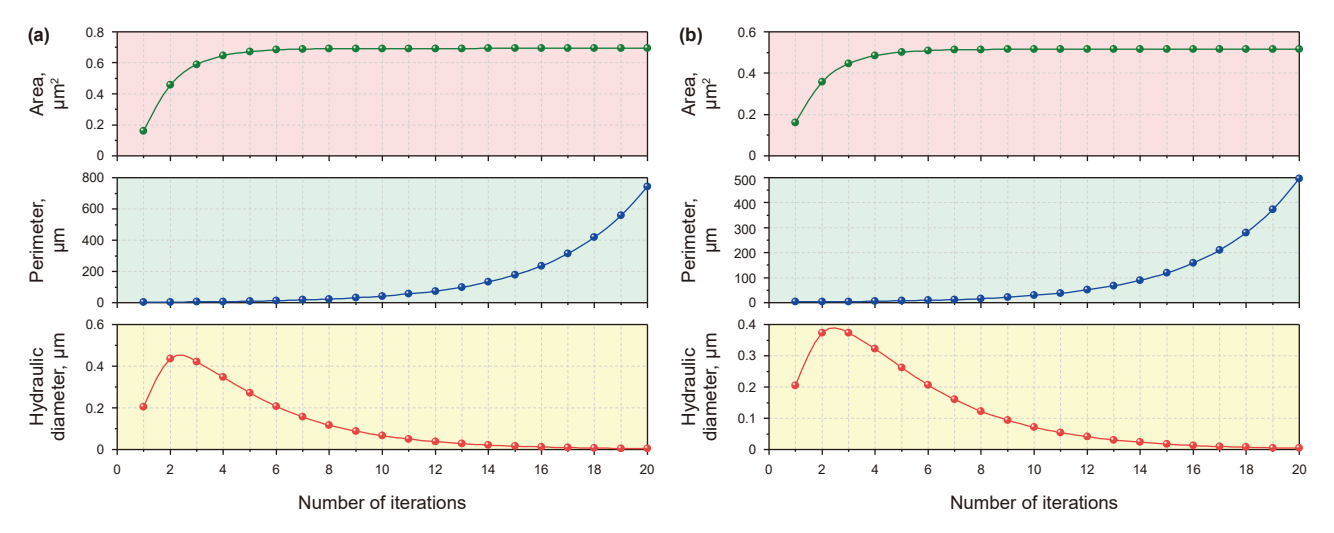


Fig. 12. Variation of the geometric parameters of the generated pores with the number of iterations ($r_0 = 1 \mu m$). (a) Unit A; (b) Unit B.

iteration number reaches a certain value, the newly generated pores have minimal areas, contributing little to the total area. In contrast, the wetted perimeter remains relatively stable initially, but increases gradually at an accelerating rate in the later stages. This can be attributed to the fact that, as iterations progress, more small pores are generated, and the number of these sub-pores increases exponentially (as shown in the second column of Appendix Table A1), leading to a sharp rise in the total perimeter. Thus, in the early stages, the area increases faster than the perimeter, while in the latter, the opposite occurs, leading to an initial rise in the hydraulic diameter of individual pores, followed by a sharp decline toward zero. This observation is consistent with the actual conditions. It is known that as the complexity of the pore cross-sectional shape increases (e.g., with more iterations), its irregularity becomes more pronounced, with many newly formed internal corners appearing. The numerous internal corners cause the previously "smooth" pore contours to become highly "winding and tortuous" due to their increased complexity. On one hand, this directly intensifies the roughness of the pore boundaries, lengthening the flow path and disrupting fluid flow, which subsequently raises viscous resistance. On the other hand, it leads to a sharp increase in the specific surface area, thereby enhancing the contact area between the pore wall and fluid, significantly strengthening frictional resistance, which in turn raises energy consumption and reduces the volumetric flow rate. Therefore, as reflected in Fig. 12, the hydraulic diameter is closely related to the pore cross-sectional shape. A greater deviation of the crosssectional shape from a circle results in a smaller hydraulic diameter, accompanied by more significant suppression in fluid flow (Zhao et al., 2021).

Fig. 13 shows the variation in shape factors generated by different IFUs as iterations progress. The shape factors of all generated pores initially increase, then decrease, and eventually stabilize. The difference is that the shape factors from Unit C and D converge to 0.436 and 0.454, respectively, while those from Unit A and B approach 0. This results from the disparities in the number of solid particles excluded from each iteration (N_n) within the IFUs. Specifically, Unit A is a pure fractal structure, where each part becomes progressively more refined and winding with each iteration, resulting in a highly intricate pore shape. This ultimately causes the hydraulic diameter and shape factor to approach 0, consistent with the trend shown in Fig. 12. For Unit B, with $N_{\rm Bn}=1$, meaning that the few non-fractal regions are insufficient to

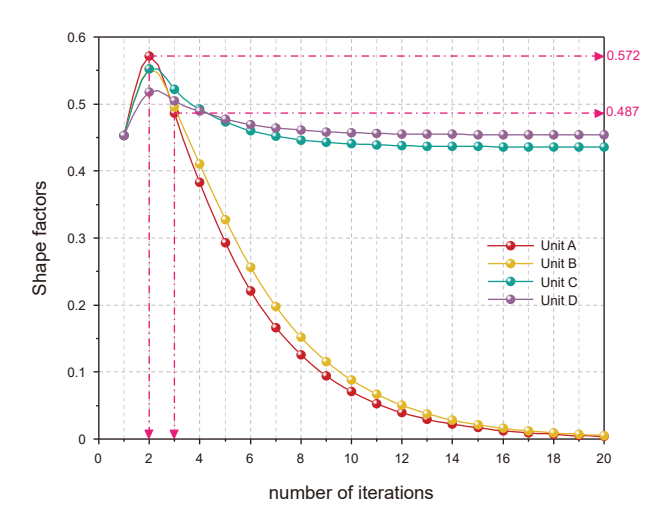


Fig. 13. Variation of shape factors of pores generated by different fractal units with the number of iterations.

significantly influence the overall complexity, resulting in a trend similar to that of Unit A. In contrast, the values of $N_{\rm n}$ for Units C and D are 3 and 4, respectively, i.e., approximately half or more of the areas are non-iterative. This suggests that as the iteration process progresses, the contribution of the relatively minor fractal areas to overall complexity becomes increasingly limited. Even with an infinite number of iterations, most pore boundaries maintain the initial "smooth" morphology. As a result, their shape factors and hydraulic diameters converge to non-zero values.

Additionally, our research shows that the number of iterations typically ranges from 2 to 3 when using IFM to invert PSD (see Table 3). Based on this, the variation range of the shape factors can be determined. As shown in Fig. 13, the final calculated shape factors for different IFUs generally range from 0.487 to 0.572, corresponding to the shape factors from Unit A when the iteration counts are 2 and 3, respectively. It is noteworthy that Benavente et al. (2002) calculated the pore shape factors for 12 different rock samples based on backscattered electron images (BSEI), with values ranging from 0.488 to 0.601 and an average of 0.531. Apparently, the range of shape factors derived from previous image analysis is highly consistent with those calculated by IFM, which further supports the practicality and convenience of the proposed model for simulating the pore structure and predicting the flow characteristics within real rocks.

In summary, determining the average pore shape factor using image analysis or other experimental methods is both labor-intensive and time-consuming (Dong et al., 2021; Qin et al., 2022). Moreover, calculating the shape factor for each individual pore is practically infeasible. In response to this challenge, the proposed IFM model simplifies complex porous media by employing multiple fractal parameters, significantly improving the efficiency of PSD reconstruction and providing quantitative information for each individual pore. Furthermore, all parameters in the model have well-defined physical meanings, which contribute to a more in-depth understanding of the mechanisms that govern two-phase flow characteristics.

4.2. Analysis of factors influencing flow behavior

The parameters in the IFM govern the PSD, thereby affecting the transport characteristics in the porous media. These parameters can be divided into two categories: fractal iteration parameters, which include the number of iterations (m) and the number of solid particles involved in each iteration (N_s) , and pore structure parameters, such as porosity (ϕ) , tortuosity fractal dimension (D_T) , and the radius of 1st-level solid particles (r_0) . To highlight the relationship between these parameters and absolute permeability, phase permeability, and relative permeability, a specific fractal unit is chosen for analysis in this section. In this case, Eqs. (24), (30), and (32) can be simplified into Eqs. (34), (35), and (36), respectively, as follows:

$$K_{a} = \frac{\pi}{32A_{t}} \sum_{i=1}^{m} \left(\frac{n_{i} \cdot d_{h}^{D_{T}+3}(i)_{m}}{L_{0}^{D_{T}-1}(D_{T}+3)(D_{T}+4)} \right)$$
(34)

$$K_{\rm W} = \frac{\pi}{32A_{\rm t}} \sum_{i=1}^{m} \left(\frac{n_i \cdot (d_{\rm h} S_{\rm w})^{D_{\rm T}+3} (i)_m}{L_0^{D_{\rm T}-1} (D_{\rm T}+3) (D_{\rm T}+4)} \right) \tag{35-1}$$

$$K_{\text{nw}} = \frac{\pi}{32A_{\text{t}}} \sum_{i=1}^{m} \left(\frac{n_{i} \cdot (d_{\text{h}} \sqrt{1 - S_{\text{w}}})^{D_{\text{T}} + 3} (i)_{m}}{L_{0}^{D_{\text{T}} - 1} (D_{\text{T}} + 3)(D_{\text{T}} + 4)} \right)$$
(35-2)

$$K_{\text{rw}} = S_W^{D_T + 3}$$
 (36-1)

$$K_{\text{rnw}} = (1 - S_{\text{W}})^{\frac{D_{\text{T}} + 3}{2}}$$
 (36-2)

Superficially, Eq. (36) suggests that relative permeability is solely a function of saturation and the tortuosity fractal dimension (D_T) . Indeed, as shown in Eq. (15), D_T itself depends on both fractal iteration and pore structure parameters. Next, we first analyze the impact of different parameters on absolute permeability using Eq. (34), followed by an examination of their effects on phase and relative permeability based on Eqs. (35) and (36), respectively.

4.2.1. Influence analysis of absolute permeability

Fig. 14 illustrates the influence of various parameters on absolute permeability. r_0 directly governs the maximum hydraulic diameter when other parameters are held constant, thus leading to a significant increase in permeability with the radius of the 1st-level solid particles, as depicted in Fig. 14(a). This is because an increase in r_0 directly raises the total number of capillaries in the porous media, thus significantly improving the seepage capacity of the reservoir (Huang et al., 2018). Moreover, combined with Fig. 14 (c), it is apparent that higher porosity has a greater effect on enhancing permeability. In fact, the positive correlation between

permeability and porosity is a commonly observed phenomenon (Nishiyama and Yokoyama, 2017; Rezaei Niya and Selvadurai, 2018). This occurs because higher porosity results in a lower solid-phase particle content in the media, which makes the flow paths more direct, thus reducing flow resistance and exhibiting stronger seepage capacity.

Fig. 14(b) shows that as the number of iterations increases. permeability initially rises and then decreases, with the maximum permeability achieved when the iteration count equals 2. The effect of the number of iterations on permeability is multifaceted. On the one hand, as iteration progresses, more pore areas are generated, leading to a rise in permeability in the early stages. On the other hand, each subsequent iteration results in a more complex cross-sectional shape, which reduces the shape factor, Eq. (33) shows that hydraulic diameter is dependent on both pore area and shape factor. As a result, the relationship between hydraulic diameter and iteration number is non-monotonic. As discussed in previous sections, hydraulic diameter is a key factor in determining the permeability of porous media (Cai et al., 2014; Dong et al., 2021). Accordingly, the changes in permeability shown in Fig. 14(b) align with the variations in hydraulic diameter presented in Fig. 12. Additionally, it is evident from the figure that permeability variation is highly responsive to r_0 , i.e., larger values of r_0 lead to more significant changes in permeability. This can be

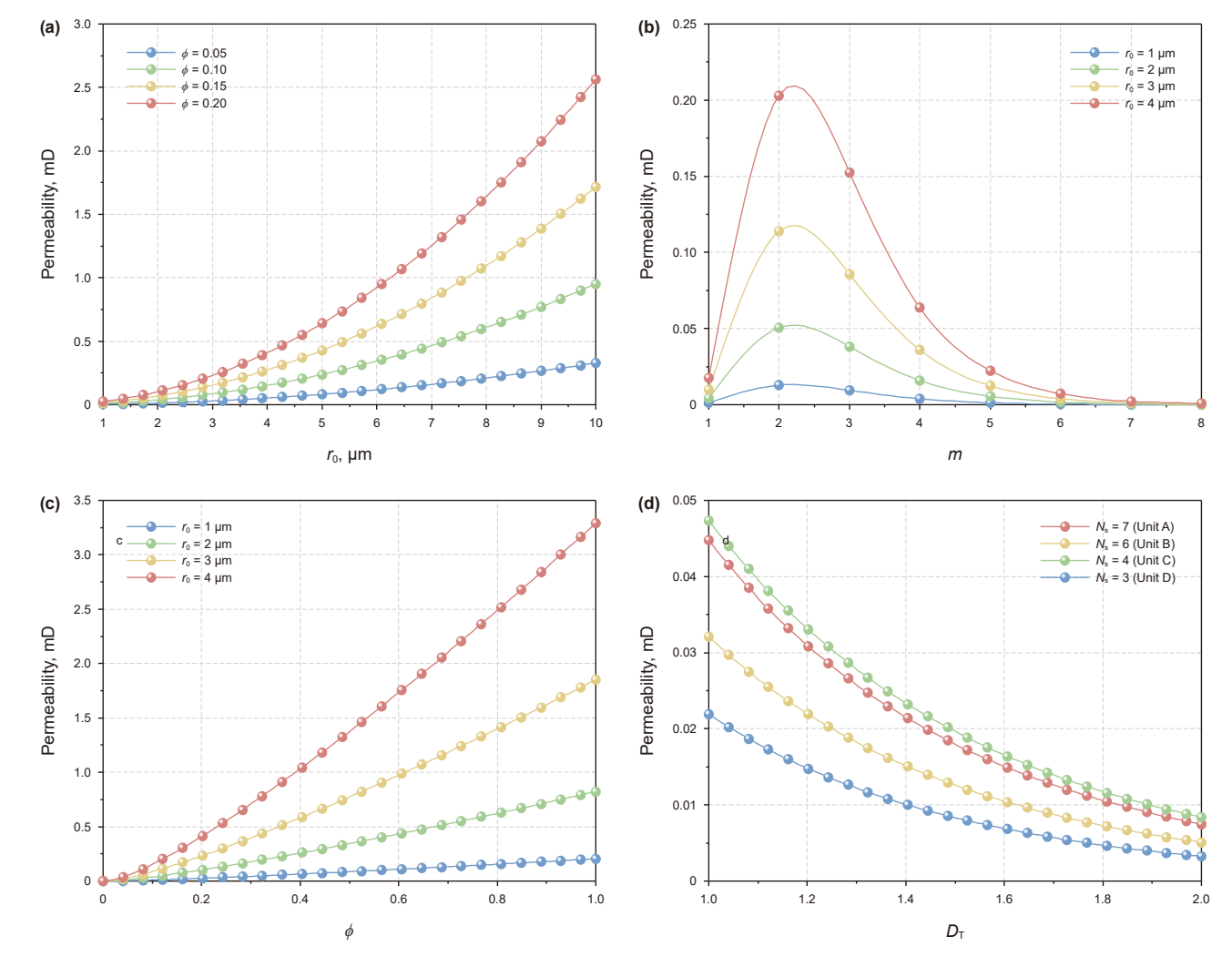


Fig. 14. Analysis of factors influencing permeability. **(a)** Effect of the 1st-level particle radius r_0 on permeability K_a at different porosity ϕ for unit A (m=3). **(b)** Effect of the number of iterations m on K_a at different r_0 for unit A $(\phi=0.1)$. **(c)** Effect of ϕ on K_a at different r_0 for unit A (m=3). **(d)** Effect of tortuosity fractal dimension D_T on K_a at different N_s $(m=4, r_0=1 \ \mu\text{m})$.

attributed to the fact that, in tight reservoirs, nanoscale pores contribute minimally to permeability, while the relatively few microscale pores, which serve as the primary flow spaces, provide the majority of the permeability (Lai et al., 2015).

Fig. 14(d) reveals the effect of tortuosity fractal dimension D_T on permeability. D_T is a crucial parameter that characterizes the heterogeneity of the reservoir. A larger D_T indicates more tortuous flow paths and higher flow resistance, resulting in a decrease in permeability. The effect of N_s on permeability should be considered in conjunction with the number of iterations. When other parameters are fixed, a larger N_s leads to the generation of more pores and a larger pore area in each iteration. Specifically, when considering pore generation capacity alone, the order is Unit A > Unit B > Unit C > Unit D. Moreover, due to the varying structures of the IFUs, the complexity of the cross-sectional shapes generated during iterations also differs. As shown in Fig. 13, when the number of iterations is four, the order of shape factors for each fractal unit is: Unit D > Unit C > Unit B > Unit A. Eventually, under the combined influence of both pore area and shape factor, as shown in Fig. 14(d), Unit C, which has the lesser pore-generating capacity, exhibits the highest permeability. In contrast, Unit A, with the largest pore area, has a relatively lower permeability than the former.

The above analysis suggests that the value of permeability is a comprehensive reflection of the interaction among various factors. The proposed model links different parameters to the macroscopic physical properties of reservoir rocks and effectively illustrates the mechanism of micro-pore structure characteristics influencing permeability.

4.2.2. Influence analysis of phase and relative permeability

Fig. 15 shows the influence of various parameters on absolute and relative permeability. A common feature among the four subplots is that, at low wetting phase saturation, the phase permeability of the wetting fluid initially increases slowly. Subsequently, as the saturation surpasses a certain threshold, the increase in its phase permeability accelerates significantly. This arises from the distribution of the wetting and non-wetting phases in the rock. Specifically, at low wetting phase saturation, the wetting fluid is primarily distributed at the edges of the pore channels, while the non-wetting phase occupies most of the central pore space, resulting in low continuity of wetting phase flow. Once the saturation exceeds a certain critical value, the flow continuity improves dramatically. In this case, the wetting phase gradually fills the primary flow channels, leading to a rapid

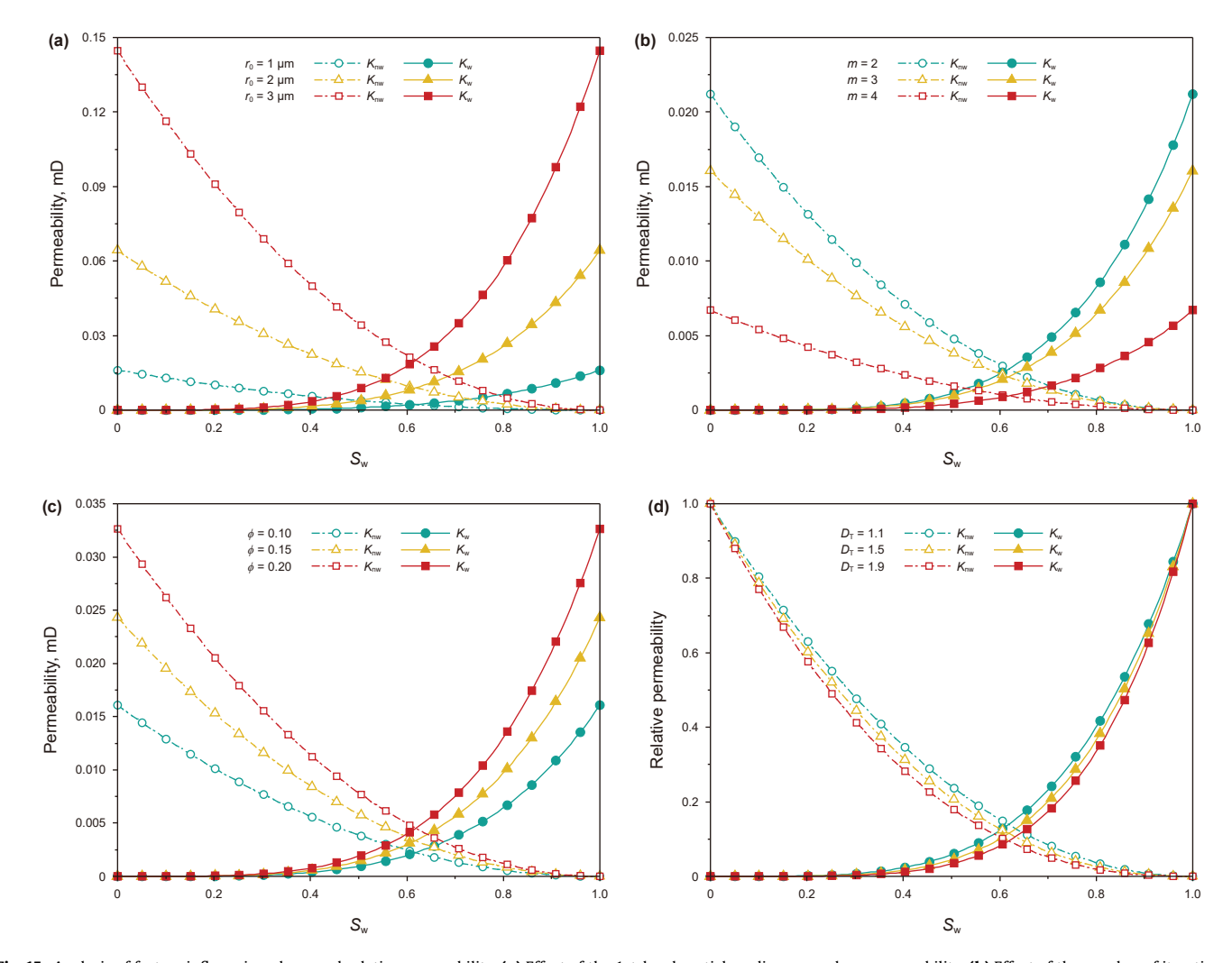


Fig. 15. Analysis of factors influencing phase and relative permeability. (a) Effect of the 1st-level particle radius r_0 on phase permeability. (b) Effect of the number of iterations m on phase permeability. (c) Effect of porosity ϕ on phase permeability. (d) Effect of tortuosity fractal dimension D_T on relative permeability.

increase in its phase or relative permeability. This pattern, in turn, reflects the "annular flow" assumption in the presented model.

With $\phi=0.1$ and m=3, the effect of the 1st-level particle radius r_0 on two-phase seepage characteristics is investigated, as shown in Fig. 15(a). The value of r_0 determines the apparent volume of the porous media. When other parameters are fixed, a larger r_0 results in wider pore channels and lower flow resistance, enhancing the phase permeability of both wetting and non-wetting fluids. Moreover, as r_0 increases, the changes in phase permeability become more pronounced, since the development of larger pores is the decisive factor in enhancing permeability (Lai et al., 2015), as discussed earlier.

The number of iterations governs the complexity of the pore structure generated by the model. Let $\phi=0.1$ and $r_0=1~\mu m$. Fig. 15 (b) depicts the phase permeability of wetting and non-wetting fluids versus saturation at varying iteration counts. Clearly, as the iteration count increases, the phase permeability of the two-phase fluids declines, a finding also supported by Figs. 13 and 14 (a). Explicitly, once the iterations exceed 2, the increase in pore area growth rate is slower than that of the wetted perimeter, leading to a higher shape factor and a smaller hydraulic diameter, which ultimately lowers the phase permeability of the two-phase fluids.

Fig. 15(c) shows the effect of the porosity on phase permeability. Given $r_0 = 1 \mu m$, m = 3, and porosities of 0.1, 0.15, and 0.2, respectively, the figure illustrates a positive correlation between porosity and phase permeability. As mentioned previously, greater porosity facilitates fluid transport through the porous media, thereby resulting in lower flow resistance and higher phase permeability.

The tortuosity fractal dimension $D_{\rm T}$ is a key parameter affecting two-phase flow characteristics. A $D_{\rm T}$ value of 1 implies that the flow path or seepage channel is straight. A greater $D_{\rm T}$ value indicates an elevated degree of capillary curvature (Yu et al., 2014) and a higher proportion of small pores (Wang et al., 2019). Fig. 15 (d) illustrates the relative permeabilities versus wetting phase saturation at different tortuosity fractal dimensions. The results reveal that $D_{\rm T}$ markedly affects relative permeability. As $D_{\rm T}$ increases, the microcosmic pore structure grows more complex, resulting in longer effective flow paths for fluid motion. This intensifies the nonlinearity of seepage, which in turn leads to a reduction in the relative permeability of the two-phase fluids.

In conclusion, the proposed model provides a comprehensive insight of the primary controlling factors governing two-phase flow in reservoirs, offering theoretical support for the efficient development and utilization of tight oil and gas resources. However, it should be noted that this model is theoretically based on fractal theory and Darcy's law, making it applicable exclusively to the dynamics of Newtonian fluids within fractal porous media.

5. Conclusions

In this study, recognizing that the PSD in dense porous media exhibits diverse fractal characteristics, we introduce intermingled fractal theory to achieve an accurate simulation of the real pore structure. On this basis, a new IFM is developed to capture the geometric shapes of the pores, and further research is conducted on the flow characteristics of both single-phase and two-phase fluids. The key findings are as follows:

 The well-designed IFM effectively matches observed physical phenomena; that is, as the resolution increases, more details of the pore cross-sections are revealed. Then, predictions of permeability are made, with the model's results validated against the measured data. The results show that the calculations exhibit strong agreement with the experimental ones, with a relative error within 10%. By contrast, the classical Pia model, which ignores geometric shapes, demonstrates a larger prediction error. This indicates that the geometric shape of pores has a significant impact on flow characteristics in tight reservoirs and cannot be overlooked.

- 2) With increasing iterations, the geometric factor initially increases, subsequently decreases, and eventually stabilizes. The geometric factor peaks at an iteration count of 2. The results of reconstructing the actual PSD via the IFM reveal that the geometric factor of pores ranges from 0.487 to 0.572, which is consistent with the shape factor range previously established by image analysis.
- 3) The newly proposed relative permeability model is a function of the wetting phase saturation, fractal iteration parameters (including the number of fractal units, iteration counts, and number of solid particles involved in each iteration), and pore structure parameters (such as porosity, solid particle radius, hydraulic diameter, and tortuosity fractal dimension). Every parameter in the model possesses a well-defined physical significance. A comparison is conducted between the model's predictions and those of published classical models, demonstrating its superior predictive accuracy.
- 4) The influence of various types of parameters on flow behavior is examined. Higher porosity and larger solid particle size markedly enhance the phase permeability. When the number of iterations exceeds two, any further iterations lead to greater complexity in the shape of the pore cross-section, which in turn results in a reduction of two-phase seepage capacity. Additionally, a higher tortuosity fractal dimension leads to more tortuous flow paths and greater seepage resistance, thereby decreasing the relative permeability of both wetting and nonwetting phases.

CRediT authorship contribution statement

You Zhou: Writing – original draft, Validation, Writing – review & editing, Methodology. **Song-Tao Wu:** Writing – review & editing, Methodology, Resources. **Ru-Kai Zhu:** Investigation, Resources, Methodology. **Xiao-Hua Jiang:** Investigation, Data curation. **Gan-Lin Hua:** Investigation, Data curation.

Declaration of competing interest

The authors declare that they have no known competing financial interests or personal relationships that could have appeared to influence the work reported in this paper.

Acknowledgments

This work was financially supported by the Hebei Provincial Natural Science Foundation of China (No. D2023402012) and the Major Science and Technology Project of China National Petroleum Corporation (No. 2024DJ87).

Appendix A. Supplementary data

Supplementary data to this article can be found online at https://doi.org/10.1016/j.petsci.2025.06.011.

References

- Afagwu, C., Alafnan, S., Mahmoud, M.A., et al., 2024. Permeability modeling of pore shapes, compaction, sorption, and molecular diffusivity in unconventional reservoirs. SPE J. 29 (5), 2729–2747. https://doi.org/10.2118/219460-PA.
- Atzeni, C., Pia, G., Sanna, U., 2008. Fractal modelling of medium-high porosity SiC ceramics. J. Eur. Ceram. Soc. 28 (14), 2809–2814. https://doi.org/10.1016/j.jeurceramsoc.2008.03.039.
- Benavente, D., Lock, P., Ángeles García Del Cura, M., et al., 2002. Predicting the capillary imbibition of porous rocks from microstructure. Transp. Porous Med. 49, 59–76. https://doi.org/10.1023/A:1016047122877.
- Brun, M., Casnedi, L., Pia, G., 2018. Bending strength of porous ceramics tiles: bounds and estimates of effective properties of an intermingled fractal units' model. Ceram. Int. 44 (9), 10241–10248. https://doi.org/10.1016/j. ceramint.2018.03.028.
- Cai, J.C., Perfect, E., Cheng, C.L., et al., 2014. Generalized modeling of spontaneous imbibition based on Hagen–Poiseuille flow in tortuous capillaries with variably shaped apertures. Langmuir 30 (18), 5142–5151. https://doi.org/10.1021/la5007204
- Casnedi, L., Licheri, R., Brun, M., et al., 2020. From nature geometry to material design: advanced fractal nature analysis for predicting experimental elastic properties. Ceram. Int. 46 (15), 23947–23955. https://doi.org/10.1016/j.ceramint.2020.06.171.
- Chai, X.L., Tian, L., Wang, J.X., et al., 2024. A novel prediction model of oil-water relative permeability based on fractal theory in porous media. Fuel 372, 131840. https://doi.org/10.1016/j.fuel.2024.131840.
- Chen, H., Chen, K., Yang, M.H., et al., 2020. A fractal capillary model for multiphase flow in porous media with hysteresis effect. Int. J. Multiph. Flow 125, 103208. https://doi.org/10.1016/j.ijmultiphaseflow.2020.103208.
- Dong, C.L., Teng, T., Li, Z.H., et al., 2021. Theoretical model of water spontaneous imbibition of sandstone considering microscopic pore geometry. J. Min. Sci. Technol. 6 (4), 418–428. https://doi.org/10.19606/j.cnki.jmst.2021.04.006 (in Chinese).
- Fu, W., Hu, W.S., Yi, T.S., et al., 2022. Fractal dimension analysis of pores in coal reservoir and their impact on petrophysical properties: a case study in the Province of Guizhou, SW China. Minerals 12 (11), 1425. https://doi.org/ 10.3390/min12111425.
- Huang, S., Yao, Y.D., Zhang, S., et al., 2018. A fractal model for oil transport in tight porous media. Transp. Porous Med. 121, 725–739. https://doi.org/10.1007/ s11242-017-0982-1.
- Juri, J.E., Dijke, M.I.J., Sorbie, K.S., 2016. Inversion of the lattice network wettability subjected to the capillary pressure of the entire flooding cycle: hamiltonian Monte Carlo posterior sampling and prediction of the relative permeability. J. Pet. Sci. Eng. 146, 1037–1062. https://doi.org/10.1016/j. petrol 2016 07 006
- Kim, S., Zhang, J.T., Ryu, S., 2023. Experimental study: the effect of pore shape, geometrical heterogeneity, and flow rate on the repetitive two-phase fluid transport in microfluidic porous media. Micromachines 14 (7), 1441. https://doi.org/10.3390/mi14071441.
- Kong, D.S., Zhao, M.K., Teng, S., et al., 2023. Stress-dependent fractal model for predicting the relative permeability of rocks based on equivalent capillaries. Ind. Eng. Chem. Res. 62 (51), 22071–22080. https://doi.org/10.1021/acs. jecr.3c02961.
- Lai, J., Wang, G.W., Meng, C.Q., et al., 2015. Pore structure characteristics and formation mechanisms analysis of tight gas sandstones. Prog. Geophys. 30 (1), 217–227. https://doi.org/10.6038/pg20150133 (in Chinese).
- Lewis, A.M., Boose, E.R., 1995. Estimating volume flow rates through xylem conduits. Am. J. Bot. 82 (9), 1112–1116. https://doi.org/10.1002/j.1537-2197.1995.
- Li, C.X., Lin, M., Ji, L.L., et al., 2018. Rapid evaluation of the permeability of organic-rich shale using the 3D intermingled-fractal model. SPE J. 23 (6), 2175–2187. https://doi.org/10.2118/191358-PA.
- Li, C.X., Xian, C.G., Ge, H.K., et al., 2022a. The mechanism analysis for hemiwicking on spontaneous imbibition in tight sandstone based on intermingled fractal model. J. Pet. Sci. Eng. 213, 110437. https://doi.org/10.1016/j.petrol.2022.110437.
- Li, F.X., Zeng, F.H., Shen, Y.Q., et al., 2022b. A fractal relative permeability model for two-phase flow through unsaturated shale porous medium. Front. Earth Sci. 10, 1009750. https://doi.org/10.3389/feart.2022.1009750.
- Li, G.Q., Su, Y.L., Wang, W.D., 2023. The fractal mathematical models for spontaneous and forced imbibition with different cross-section shapes in shale oil reservoir. Fractals 31, 2350002. https://doi.org/10.1142/S0218348X23500020.
- Li, Y., Lei, Q., Liu, X.G., et al., 2011. Characteristics of micro scale nonlinear filtration. Petrol. Explor. Develop. 38 (3), 336–340. https://doi.org/10.1016/S1876-3804 (11)60036-0.
- Liao, Z., Detwiler, R.L., Cookson, E.S., et al., 2024. Quantitative visualization of two-phase flow in a fractured porous medium. Water Resour. Res. 60 (4), e2023WR035806. https://doi.org/10.1029/2023WR035806.
- Liu, L.L., Sun, Q.C., Wu, N.Y., et al., 2021. Fractal analyses of the shape factor in Kozeny-Carman equation for hydraulic permeability in hydrate-bearing sediments. Fractals 29 (7), 2150217. https://doi.org/10.1142/S0218348X21502170
- ments. Fractals 29 (7), 2150217. https://doi.org/10.1142/S0218348X21502170.

 Ma, H., Kinzer-Ursem, T.L., Linnes, J.C., 2024. Two-phase porous media flow model based on the incompressible Navier-Stokes equation. Anal. Chem. 96 (13), 5265–5273. https://doi.org/10.1021/acs.analchem.3c05982.

Mortensen, N.A., Okkels, F., Bruus, H., 2005. Reexamination of Hagen-Poiseuille flow: shape dependence of the hydraulic resistance in microchannels. Phys. Rev. E 71, 057301. https://doi.org/10.1103/PhysRevE.71.057301.

- Nimvari, M.E., Persoons, T., Gibbons, M., 2024. Pore-scale simulation of two-phase flow in biporous media. Phys. Fluids 36 (10), 107157. https://doi.org/10.1063/5.0232694.
- Nishiyama, N., Yokoyama, T., 2017. Permeability of porous media: role of the critical pore size. JGR Solid Earth 122 (9), 6955–6971. https://doi.org/10.1002/2016IB013793
- Niu, D.T., Li, D., Fu, Q., 2020. A 3D-IFU model for characterising the pore structure of hybrid fibre-reinforced concrete. Mater. Des. 188, 108473. https://doi.org/ 10.1016/j.matdes.2020.108473.
- Pia, G., Sanna, U., 2013. A geometrical fractal model for the porosity and thermal conductivity of insulating concrete. Constr. Build. Mater. 44, 551–556. https://doi.org/10.1016/j.conbuildmat.2013.03.049.
- Pia, G., Sanna, U., 2014a. An intermingled fractal units model to evaluate pore size distribution influence on thermal conductivity values in porous materials.
 Appl. Therm. Eng. 65 (1-2), 330-336. https://doi.org/10.1016/j.applthermaleng.2014.01.037.
 Pia, G., Sanna, U., 2014b. An intermingled fractal units model and method to
- Pia, G., Sanna, U., 2014b. An intermingled fractal units model and method to predict permeability in porous rock. Int. J. Eng. Sci. 75, 31–39. https://doi.org/ 10.1016/i.jiengsci.2013.11.002.
- Pia, G., Casnedi, L., Sanna, U., 2015a. Porous ceramic materials by pore-forming agent method: an intermingled fractal units analysis and procedure to predict thermal conductivity. Ceram. Int. 41 (5), 6350–6357. https://doi.org/10.1016/j.ceramint.2015.01.069.
- Pia, G., Casnedi, L., Ionta, M., et al., 2015b. On the elastic deformation properties of porous ceramic materials obtained by pore-forming agent method. Ceram. Int. 41 (9), 11097–11105. https://doi.org/10.1016/j.ceramint.2015.05.057.
 Pia, G., Casnedi, L., Ricciu, R., et al., 2016a. Thermal properties of porous stones in
- Pia, G., Casnedi, L., Ricciu, R., et al., 2016a. Thermal properties of porous stones in cultural heritage: experimental findings and predictions using an intermingled fractal units model. Energy Build. 118, 232–239. https://doi.org/10.1016/j. enbuild.2016.03.011.
- Pia, G., Siligardi, C., Casnedi, L., et al., 2016b. Pore size distribution and porosity influence on sorptivity of ceramic tiles: from experimental data to fractal modelling. Ceram. Int. 42 (8), 9583–9590. https://doi.org/10.1016/j. ceramint.2016.03.041.
- Pia, G., 2016. Fluid flow in complex porous media: experimental data and IFU model predictions for water vapour permeability. J. Nat. Gas Sci. Eng. 35, 283–290. https://doi.org/10.1016/j.jngse.2016.08.053.
- Pia, G., Casnedi, L., 2017. Heat transfer in high porous alumina: experimental data interpretation by different modelling approaches. Ceram. Int. 43 (12), 9184–9190. https://doi.org/10.1016/j.ceramint.2017.04.071.
- Pia, G., Gualtieri, M.L., Casnedi, L., et al., 2018. Microstructural evolution in porous ceramics subjected to freezing-thawing cycles: Modelling experimental outcomes. Ceram. Int. 44 (14), 16992–16998. https://doi.org/10.1016/j. ceramint.2018.06.141.
- Pickard, W.F., 1981. The ascent of sap in plants. Prog. Biophys. Mol. Biol. 37, 181–229. https://doi.org/10.1016/0079-6107(82)90023-2.
- Qiao, X.W., Shen, Y.Q., Tan, X.H., et al., 2022. The correlation between fluid flow and heat transfer of unsaturated shale reservoir based on fractal geometry. Fractals 30 (3), 2250069. https://doi.org/10.1142/S0218348X22500694.
- Qin, X.J., Xia, Y.X., Wu, J.S., et al., 2022. Influence of pore morphology on permeability through digital rock modeling: new insights from the Euler number and shape factor. Energy Fuels 36 (14), 7519–7530. https://doi.org/10.1021/acs.energyfuels.2c01359.
- Qiu, C., Yang, Y.G., Huang, B.X., et al., 2024. A multifractal model for predicting the permeability of dual-porosity media with rough-walled fractures and variable cross-sectional pore channels. Phys. Fluids 36 (6), 063603. https://doi.org/ 10.1063/5.0206123.
- Rezaei Niya, S.M., Selvadurai, A.P.S., 2018. A statistical correlation between permeability, porosity, tortuosity and conductance. Transp. Porous. Med. 121, 741–752. https://doi.org/10.1007/s11242-017-0983-0.
- Shi, J.T., Sun, Z., Wu, K.L., et al., 2019. Effect of pore shape on nanoconfined gas flow behavior: implication for characterizing permeability of realistic shale matrix. Ind. Eng. Chem. Res. 58 (20), 8835–8846. https://doi.org/10.1021/acs. iecr.9b00532.
- Su, H.B., Zhang, Y.D., Xiao, B.Q., et al., 2021. A fractal-Monte Carlo approach to model oil and water two-phase seepage in low-permeability reservoirs with rough surfaces. Fractals 29 (1), 2150003. https://doi.org/10.1142/ S0218348X21500031.
- Sun, H., Xiong, F., Wang, S.Y., et al., 2025. Instability mechanism and a fractal theory-based relative permeability model of immiscible two-phase displacement in rough fractures. Phys. Fluids 37 (1), 012116. https://doi.org/10.1063/5.0251082.
- Tian, X.F., Cheng, L.S., Yan, Y.Q., et al., 2015. An improved solution to estimate relative permeability in tight oil reservoirs. J. Petrol. Explor. Prod. Technol. 5, 305–314. https://doi.org/10.1007/s13202-014-0129-7.
- Wang, D.X., Hu, H.Y., Wang, T., et al., 2024. Difference between of coal and shale pore structural characters based on gas adsorption experiment and multi-fractal analysis. Fuel 371, 132044. https://doi.org/10.1016/j.fuel.2024.132044.
- Wang, F.Y., Jiao, L., Zhao, J.Y., et al., 2019. A more generalized model for relative permeability prediction in unsaturated fractal porous media. J. Nat. Gas Sci. Eng. 67, 82–92. https://doi.org/10.1016/j.jngse.2019.04.019.

- Wang, F.Y., Liu, Z.C., Yue, H., 2023. Prediction of gas—water relative permeability in tight rock from movable fluid distribution with nuclear magnetic resonance. Phys. Fluids 35 (3), 033609. https://doi.org/10.1063/5.0141543.
- Wang, F.Y., Liu, Z.C., Jiao, L., et al., 2017. A fractal permeability model coupling boundary-layer effect for tight oil reservoirs. Fractals 25 (5), 1750042. https:// doi.org/10.1142/S0218348X17500426.
- Wang, H.L., Tian, L., Gu, D.H., et al., 2020. Method for calculating non-darcy flow permeability in tight oil reservoir. Transp. Porous Med. 133, 357–372. https://doi.org/10.1007/s11242-020-01427-8.
- Wei, Z.M., Pang, Y.M., Yang, C.S., et al., 2025. Pore structure monofractal and multifractal characteristics of high-mature organic-rich shale using N₂ adsorption-desorption measurements. Nat. Resour. Res. 34, 459–482. https://doi.org/10.1007/s11053-024-10415-4.
- Wu, T., Wang, S.F., 2020. A fractal permeability model for real gas in shale reservoirs coupled with Knudsen diffusion and surface diffusion effects. Fractals 28 (1), 2050017, https://doi.org/10.1142/S0218348X20500176.
- Xiong, Y., Yu, J.B., Sun, H.X., et al., 2017. A new non-Darcy flow model for low-velocity multiphase flow in tight reservoirs. Transp. Porous Med. 117, 367–383. https://doi.org/10.1007/s11242-017-0838-8.
- Xu, P., Qiu, S.X., Yu, B.M., et al., 2013. Prediction of relative permeability in unsaturated porous media with a fractal approach. Int. J. Heat Mass Transf. 64, 829–837. https://doi.org/10.1016/j.ijheatmasstransfer.2013.05.003.
 Yang, S.S., Chen, S.Y., Yuan, X.B., et al., 2024. Relative permeability model of two-
- Yang, S.S., Chen, S.Y., Yuan, X.B., et al., 2024. Relative permeability model of twophase flow in rough capillary rock media based on fractal theory. Fractals 32 (5), 2450075. https://doi.org/10.1142/S0218348X24500750.
- Yang, Y.H., Jin, Y., Song, H.B., et al., 2025. Shape and size effects on adsorption performance of methane from pores in coal. Energy 318, 134814. https://doi. org/10.1016/j.energy.2025.134814.
- Yu, B.M., Li, J.H., 2004. A geometry model for tortuosity of flow path in porous media. Chin. Phys. Lett. 21 (8), 1569–1571. https://doi.org/10.1088/0256-307X/ 21/8/044.

- Yu, B.M., Li, J.H., Li, Z.H., et al., 2003. Permeabilities of unsaturated fractal porous media. Int. J. Multiphase Flow 29 (10), 1625–1642. https://doi.org/10.1016/ S0301-9322(03)00140-X.
- Yu, B.M., Xu, P., Zou, M.Q., 2014. Transport Physics in Fractal Porous Media. Science Press (in Chinese).
- Yu, S.Q., Kang, Q.J., Mehana, M., 2024. Quantifying the effect of pore-size dependent wettability on relative permeability using capillary bundle model. JGR Solid Earth 129, e2024|B028674. https://doi.org/10.1029/2024|B028674.
- Yun, M.J., Yu, B.M., Xu, P., et al., 2006. Geometrical models for tortuosity of streamlines in three-dimensional porous media. Can. J. Chem. Eng. 84 (3), 301–309. https://doi.org/10.1002/cjce.5450840305.
- Zhang, H.T., Luo, X.Q., Bi, J.F., et al., 2018. Multi-component fractal representation of multi-scale structure of natural gas hydrate-bearing sediments. J. Nat. Gas Sci. Eng. 60, 144–152. https://doi.org/10.1016/j.jngse.2018.10.015.
- Zhao, M.K., Kong, D.S., Shi, J., et al., 2024. A coupled fractal model for predicting the relative permeability of rocks considering both irreducible fluid saturation and stress effects. Phys. Fluids 36, 103342. https:// doi.org/10.1063/5.0232292.
- Zhao, Z.X., He, J.J., Wang, C., 2021. Hydraulics, third ed. Tsinghua University Press (in Chinese).
- Zhou, Y., Wu, S.T., Li, Z.P., et al., 2018. Multifractal study of three-dimensional pore structure of sand-conglomerate reservoir based on CT images. Energy Fuels 32 (4), 4797–4807. https://doi.org/10.1021/acs.energyfuels.8b00057.
- Zhou, Y., Wu, S.T., Li, Z.P., et al., 2021. Investigation of microscopic pore structure and permeability prediction in sand-conglomerate reservoirs. J. Earth Sci. 32 (4), 818–827. https://doi.org/10.1007/s12583-020-1082-7.
- Zhou, Y., Wu, S.T., Zhu, R.K., et al., 2025. A new model for determining the effective permeability of tight reservoirs based on Fractal-Monte Carlo method. Pet. Sci. 22 (8), 3101–3118. https://doi.org/10.1016/j.petsci.2025.04.016.